TECHNISCHE UNIVERSITÄT WIEN

DIPLOMARBEIT

"Laser-induced breakdown spectroscopy of copper, nickel and nickel-phosphorus coatings: Influence of laser wavelength"

Ausgeführt am Institut für
Physikalische Chemie
der Universität Wien
unter der Anleitung von Univ.-Prof. Dr. Wolfgang Kautek

eingereicht an der Technischen Universität Wien durch
Evgeniya Paulis, BSc

Anschrift: Heckenweg 57, 1220 Wien

October 30, 2017

Personal information:
Official working group adress: IPC, nano [online, October 30, 2017]
Company Website

Licence:

Abstract

Laser-induced breakdown spectroscopy (LIBS) was demonstrated for depth profiling of model coating systems on steel such as copper, nickel and nickel-phosphorous. A Nd:YAG laser emitting at 1064 nm (pulse duration 7 ns), and at 532 nm (pulse duration 5 ns) was employed. The measured spectra were analysed with the Pearson linear correlation.

The incubation, the increase of ablation rate and the decrease of the ablation threshold fluence with the pulse number, is comparatively low for all coating systems. That indicates, that the defects density responsible for this phenomenon is intrinsically high in these galvanic and electroless samples so that repeated pulsing does not lead to a drastic further defect density increase.

The ablation rate depends strongly on the wavelength. This cannot be explained by the optical absorption of the substrates. The thermal diffusion length together with plasma shielding can explain the observed behaviour semi-quantitatively. Plasma shielding affects the ablation process with the near-infrared wavelength in contrast to the visible case where it is negligible.

These results show that the beam-plasma interaction not only plays an important role in the quantification of the ablation rate, the depth resolution and the analysis depth, but also in the plasma heating which itself affects the plasma emission efficiency. Thus, plasma shielding supports a higher depth resolution paralleled by a sensitivity increase due to plasma heating. Normally, a high stratigraphic resolution (low ablation rate) and a strong emission signal due to a high plasma volume and temperature exclude each

other. However, the absorption of the plasma both reduces the fluence on the sample and the ablation rate, and heats the plasma, resulting in a higher emission efficiency.

Zusammenfassung

Laser-induced Breakdown Spectroscopy (LIBS) wurde für die Tiefenprofilanalyse von Modellbeschichtungssystemen wie Kupfer, Nickel und Nickelphosphor auf Stahl untersucht und entwickelt. Zum Einsatz kam ein Nd:YAG-Laser, der entweder bei 1064 nm (Pulsdauer 7 ns) oder bei 532 nm (Pulsdauer 5 ns) emittierte. Die gemessenen Spektren wurden mit der linearen Pearson-Korrelation analysiert. Die Inkubation, die Erhöhung der Abtragsrate (Ablationsrate) und die Verringerung der Ablationsschwellenfluenz mit der Pulszahl, war bei allen Beschichtungssystemen verhältnismäßig gering. Das deutet darauf hin, dass die für dieses Phänomen verantwortliche Defektdichte in diesen galvanischen und stromlos abgeschiedenen Proben intrinsisch hoch ist, so dass wiederholtes Pulsen nicht zu einer drastischen weiteren Erhöhung der Defektdichte führte.

Die Ablationsrate hing stark von der Wellenlänge ab. Dies hängt jedoch nicht mit der optischen Absorption der Substrate zusammen. Die thermische Diffusionslänge und die Plasmaabschirmung können dagegen das beobachtete Verhalten semi-quantitativ erklären. Plasmaabschirmung wirkt sich auf den Ablationsprozess im nahen Infrarot-Wellenlängenbereich aus. Im Gegensatz dazu ist die Abschirmung bei sichtbarer Laserstrahlung vernachlässigbar. Diese Ergebnisse zeigen, dass die Laserstrahl-Plasma-Wechselwirkung nicht nur bei der Quantifizierung der Ablationsrate, der Tiefenauflösung und der Analysentiefe eine wichtige Rolle spielt, sondern auch bei der Plasmaerhitzung, die wiederum einen Einfluss auf die Plasmaemissionseffizienz hat. Die Plas-

maerhitzung unterstützt somit eine bessere Tiefenauflösung bei gleichzeitiger Erhöhung der Empfindlichkeit. Normalerweise schließen sich eine hohe stratigraphische Auflösung (niedrige Ablationsrate) und ein starkes Emissionssignal aufgrund eines hohen Plasmavolumens und einer hohen Plasmatemperatur gegenseitig aus. Die Plasmaabsorption verringert jedoch sowohl die Fluenz auf der Probe als auch die Ablationsrate und heizt das Plasma auf, was zu einer höheren Emissionseffizienz führt.

Contents

Chapter 1

Introduction

Laser-induced breakdown spectroscopy (LIBS) or sometimes called laser-induced plasma spectroscopy (LIPS) is a type of atomic emission spectroscopy, in which a laser pulse is used as an excitation source. A pulsed laser beam is focused onto a sample surface, where it vaporizes, atomizes and excites a material, creating a plasma. The plasma light is collected and spectrally analysed [1–5].

This is in contrast to common inductively coupled plasma atomic emission (ICP-OES) spectroscopy where the sample has to be dissolved in a solvent and then injected into a nebulizer chamber connected to an inductively coupled plasma torch where the excitation is supported by a radio frequency generator. Finally, the emitted light is analysed by a spectrometer. This shows that the sampling involves the destruction of the work peace followed by a technically complicated series of process steps. Moreover, depth profiling of solid material is thus impossible.

The range of applications of LIBS is wide due to the many advantages, such as technical simplicity, ability to detect all elements including light elements [6, 7]. It can be applied in air, but also under vacuum, or even under liquids [1, 8]. Samples –without any tedious preparation steps (see above) - of any sizes and three dimensional shapes can be analysed, because only optical

access to the sample is required [3]. It permits to apply LIBS for the quality assurance (QA) and quality control (QC) in industrial off-line and in-line applications [9]. Even a stand-off analysis is possible due to the long distance application of laser beams together with emission registration by telescopes. Thus, analyses of toxic [10], explosive [11, 12], and even extraterrestrial materials [13] are accessible.

The rapid stratigraphic 3D-analysis of metal coatings on structured samples is of substantial importance in modern industrial quality control routine. LIBS is one of the most promising options to receive fast and reliable depth profiling, i.e. stratigraphic, results [6, 14–19]. Furthermore, the knowledge of the ablation and emission properties allows for the development of custom analyses and machining approaches for layered materials [20].

In this study, technical model samples were chosen in order to investigate the influence of the laser wavelength on the elemental stratigraphy. Copper and nickel coatings were produced galvanically by a collaborating industrial partner. A nickel-phosphorous coating was prepared electroless. Electroplated copper is often used as an underplate, as decorative coating and in electronics due to its high conductivity [21]. Nickel and its alloys with phosphorous are widely used as decorative and functional coatings for the improvement of corrosive and wear resistance [22].

Two laser wavelengths were compared: the fundamental of a Nd:YAG laser at 1064 nm, and the second harmonic at 532 nm. The resulting plasma spectra were analysed using a linear correlation method [6]. For both wavelengths the absorption/ablation behaviour as well as LIBS depth profiling were studied and compared to theoretical values originating from a thermal ablation model [23].

Chapter 2

Theory

2.1 Physico-chemical processes in LIBS

2.1.1 Basics of atomic emission spectroscopy

Atomic emission spectroscopy (AES) is used for qualitative and quantitative analysis of solid, liquids and gases. It is based on the spontaneous emission of free atoms or ions after the excitation is performed by an external source of energy (arc, spark, plasma, laser). The emission originates from the transition of valence electrons between the stationary states in incompletely filled outer orbitals. Which transitions are possible can be predicted by quantum mechanic selection rules [24, 25]. The emitted radiation is elemental specific. The wavelength depends on the energy level of the excited and ground state of the specific elements (Figure 2.1). The difference in potential energy levels gives the frequency ν of the emitted electromagnetic wave:

$$E_2 - E_1 = h\nu \tag{2.1}$$

where E_2 is the energy of the excited state, E_1 is the energy of the ground state and h is the Planck constant.

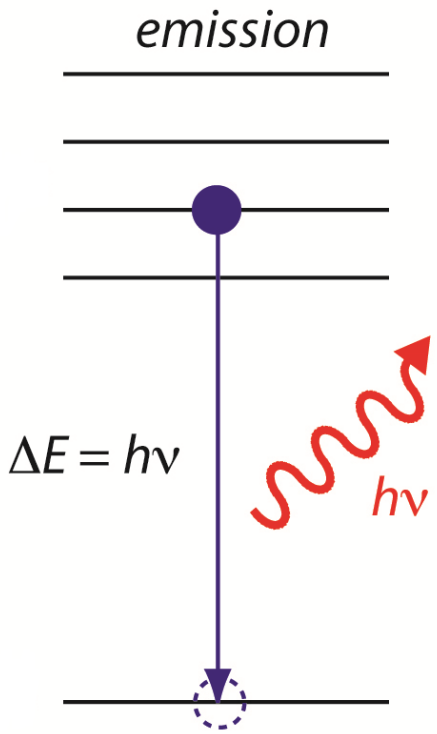

Figure 2.1: Simplified energy diagram, illustrating an electron in the excited state, releasing a photon during the transition from higher to lower energy state. (LibreTexts).

The spectral lines are broadened by several factors: natural, Doppler and collisional (Lorentzial) broadening. Natural line broadening is the consequence of a finite lifetime of an atom in any excited state. According to the Heisenberg's Uncertainty Principle, if the mean time atom spent in excited state E is Δt, there is the uncertainty ΔE in the value of E:

$$\Delta E \times \Delta t \geq \frac{h}{2\pi} \tag{2.2}$$

Natural line broadening has Lorentzial profile.

Doppler broadening is caused by the thermal movement of emitting atoms. The observer obtains the shifts corresponding to the spread of velocities in the line of sight Figure 2.2. It has Gaussian distribution.

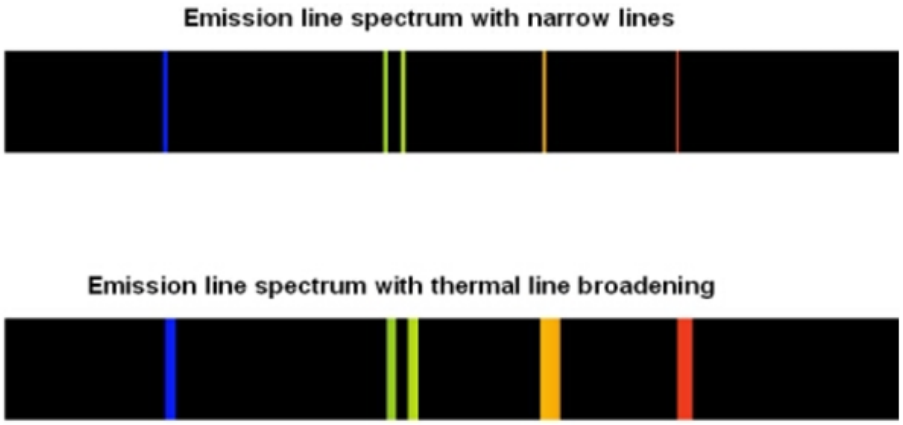

Figure 2.2: Spectrum with and without Doppler broadening (COSMOS - The SAO Encyclopedia of Astronomy).

Collision of an emitting or absorbing atom with other atoms, molecules and other particles leads also in broadening, shift, and asymmetry of the line profile. The line broadening which is directly proportional to the number of the collisions per second per atom and has Lorentzial distribution.

If both types Lorentzial and Gaussian broadening exist, the resulting line profile obtained by convolution of them is called Voigt distribution (Figure 2.3).

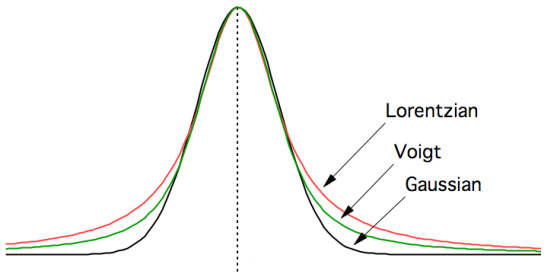

Figure 2.3: A Gaussian line width distribution profile (thermal broadening), a Lorentzial distribution profile (natural and collisional broadening) and a convolution between Gaussian and Lorentz - Voigt profile (WaveMetrics).

2.1.2 Plasma evolution

Laser beam being focused onto the material surface ignites a plasma - an assembly of atoms, free electrons and ions. The plasma is electrically neutral. The degree of ionisation (electron to atom ratio) is important plasma's characteristic.

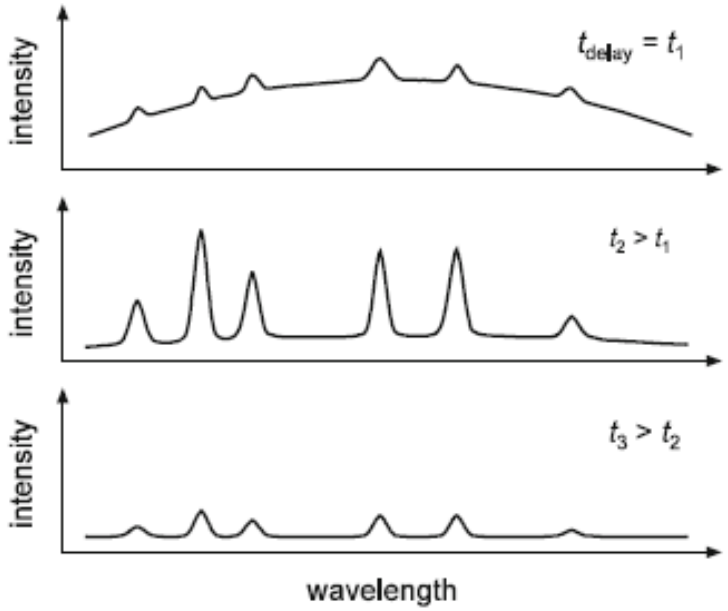

Figure 2.4: Schematic overview of a LIBS spectra measured with different time delay [4].

A schematic overview of the dependency of LIBS spectra to time delay is presented in Figure 2.4. At the time t_1 (top) the degree of ionization is high, the plasma emits continuous spectrum with only small elemental specific peaks. The continuum is caused by bremsstrahlung (free-free transition) and recombination (free-bound transition). In the bremsstrahlung free electrons hit each other and accelerates or decelerates, the excess of energy is released in the form of a photon. When a free electron attaches to an atomic/ionic level, the excess kinetic energy is emitted. This process is called recombina-

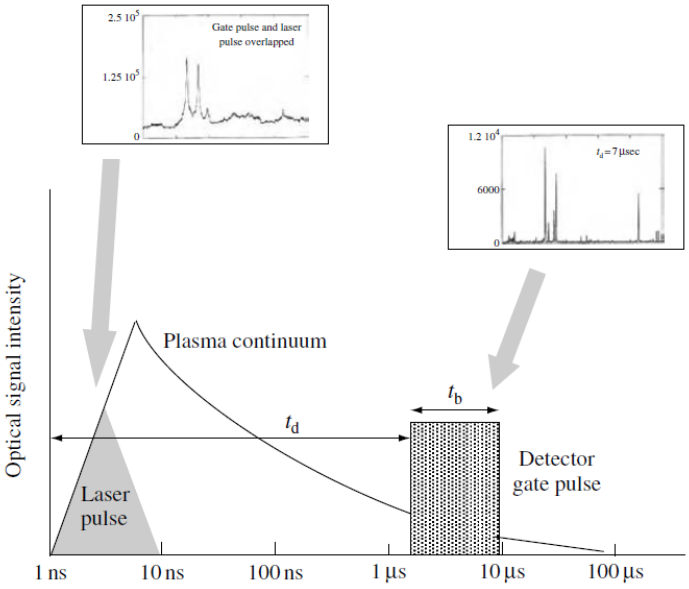

Figure 2.5: Schematic image of LIBS plasma evolution. Gate delay and integration time [2].

tion. When the plasma has cooled down (t_2), the intensity of bound-bound transition becomes higher than background emission and the characteristic elemental peaks originating from the transitions between the energy levels (bound-bound) are obtained in the spectrum. After longer period of time (t_3) plasma has cooled down more and the intensity of lines decreases.

For sufficient LIBS-analysis, it is necessary to take into account the described temporal plasma evolution. For this reason, a gating of the detector is required. The timescale of processes, taking place in plasma is presented in Figure 2.5 [2, 4]. The study of line intensity evolution process of metal samples shows the maximum at 0.75 μs for neutral atoms and 0.2 μs for ion emission lines lasting up to 10 and 5 μs respectively [26].

2.1.3 Laser-material interaction parameters

The knowledge of ablation properties of materials such as the threshold fluence, the amount of ablated material and the shape of craters is crucially important in LIBS. Generally, the ablation of materials depends on optical properties, such as adsorptivity and reflectivity, surface roughness, laser wavelength, Gaussian beam radius and pulse duration. The optical penetration depth L_{opt} can be derived by the Lambert-Beer law. It describes the length along which the laser fluence F falls to $1/\exp$ (around 37 %) of its initial value. Figure 2.6 illustrates the optical penetration depth and the heat penetration depth of laser radiation in a solid sample. After light absorption, thermal processes such as melting and mainly evaporation govern laser ablation [4, 27, 28].

In metals, the ablation rate is mainly determined by the heat penetration depth L_{th} [18, 19, 23, 29, 30]. It is a measure of the propagation length of the thermal energy into the sample . The heat penetration depth is

$$L_{\mathrm{th}} = \sqrt{2\kappa\tau} \tag{2.3}$$

$$\kappa = \frac{k}{\rho c_{\mathrm{p}}} \tag{2.4}$$

where κ is thermal diffusivity, τ is pulse duration, k is thermal conductivity, ρ density and c_{p} is heat capacity [23, 28].

An ablation threshold fluence is a minimal fluence needed to ablate the material can be defined as function of sublimation energy volume density U_{sub}, thermal diffusion length L_{th} and the reflectivity R [31]:

$$F_{\mathrm{th}} = U_{\mathrm{sub}} L_{\mathrm{th}} (1 - R)^{-1} \tag{2.5}$$

and

$$U_{\mathrm{sub}} = (L_{\mathrm{v}} + L_{\mathrm{m}})\rho \tag{2.6}$$

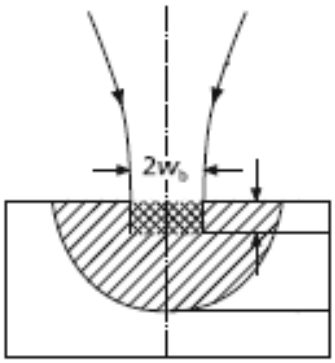

Figure 2.6: Penetration of a laser pulsed beam in a solid sample. L_{th} represent Lambert-Beer optical penetration depth, L_{th} is heat penetration depth [4].

where L_{v} is latent heat of evaporation and L_{m} is latent heat of melting. The reflectivity R and latent heat of melting can be neglected [32]:

$$F_{\mathrm{th}} = L_{\mathrm{v}} \rho L_{\mathrm{th}} \tag{2.7}$$

Assuming a Gaussian beam profile, what is applicable to the Nd:YAG laser used in this work, the radial fluence distribution is presented in Figure 2.7. If the maximal fluence F exceeds threshold fluence F_{th}, the material will be ablated and a crater with the diameter D will be formed:

$$D^2 = 2\omega_0^2 \ln \frac{F}{F_{\mathrm{th}}} \tag{2.8}$$

ω_0 is the Gaussian beam radius.

In the multi-pulse scenario the threshold fluence decreases. This phenomenon is called incubation. It can be described by a simple accumulation model:

$$F_{\mathrm{th}}(N) = F_{\mathrm{th}}(1)^{\xi - 1} \tag{2.9}$$

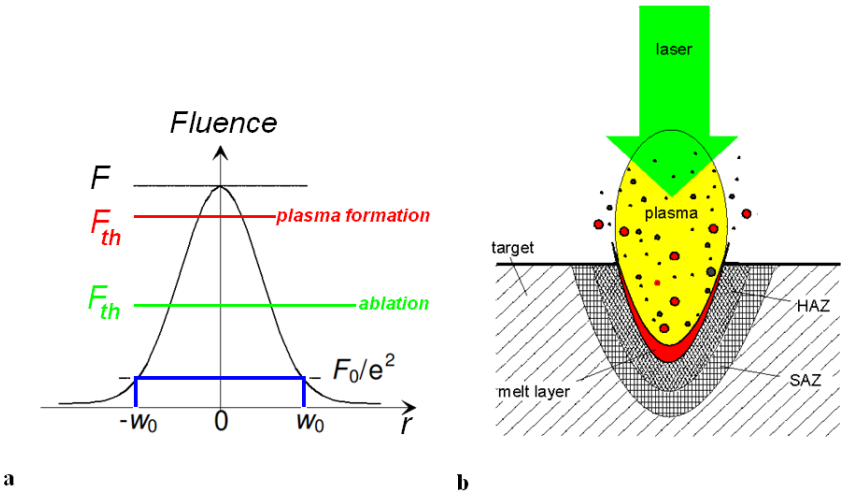

Figure 2.7: a: Fluence distribution in a Gaussian beam. F is maximal fluence, F_{th} is threshold fluence, w_0 represents Gaussian beam radius. b: Schematic image of processes taking place during the ablation solid matter by a nanosecond laser. HAZ, SAZ = heat and shock affected zone [27].

where $F_{\mathrm{th}}(N)$ is the threshold fluence at N pulse, $F_{\mathrm{th}}(1)$ threshold fluence at a single pulse [33].

The origin of the incubation is still under debate. A recent explanation is that the thermal diffusion length L_{th} is strongly decreased by the formation of defects such as nanovoids [30, 34] (compare Equation 2.5). Other hypotheses attribute the incubation of metals to the amorphisation and photothermal oxidation of a near surface layer [35–37].

Another effect to be considered is plasma shielding. Increasing the fluence, the electron density in the plasma and its absorptivity will rise [26, 38]. That can lead to a reduction of the ablation rate.

2.2 LIBS system components

In this chapter LIBS instrumentals and their physics are discussed, the state-of-art devices are listed.

A typical LIBS-setup consists of following components:

- A pulsed laser used to ignite the plasma;
- Focusing optics;
- A target holder, often mounted on a positioning device;
- A light collection system, lens, mirrors or fibers, that are used to collect the plasma spark and transport it to detection system;
- Detection system (combination of spectrograph and detector);
- Different electronics to control the laser and gate the detector.

The component specification can be tailored to the particular application [2]. All parts of the typical setup are described in the following subsections.

2.2.1 Laser

The term laser is an acronym for light amplification by stimulated emission of radiation. The principle of stimulated emission was postulated by Einstein [39].

All atomic system can exist in discrete energy states E. Assuming that the atom is initially in the excited level 2 (Figure 2.8), it will tend to decay to the energy level 1. The energy difference will be emitted in the form of an electromagnetic wave. The frequency or the wavelength of photon emitted is described by equation:

$$E_2 - E_1 = h\nu \tag{2.10}$$

where E_2 is the energy of excited level, E_1 is the energy of ground level, ν is the frequency of radiated wave, h is Planck's constant.

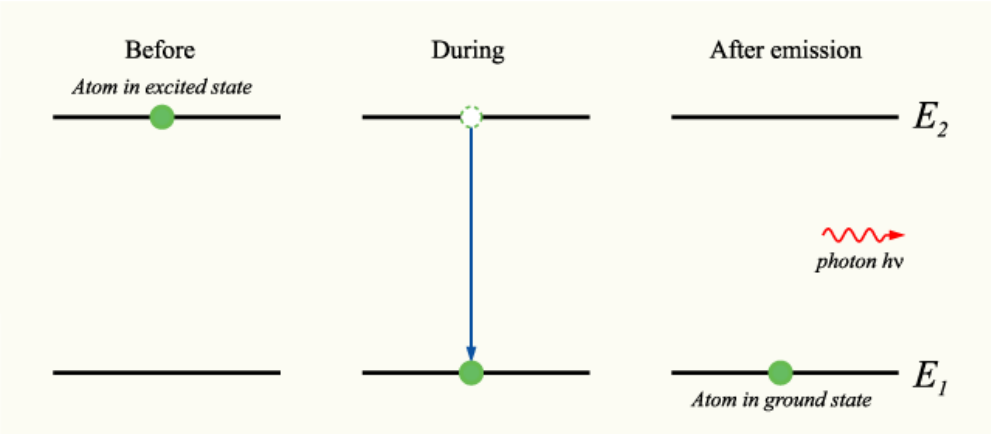

Figure 2.8: Spontaneous emission (Wikipedia).

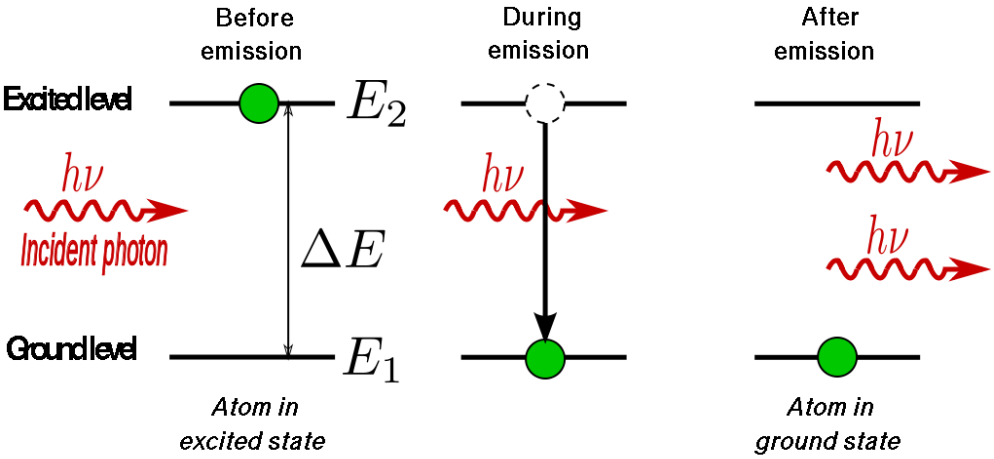

Figure 2.9: Stimulated emission (Wikipedia).

If an electromagnetic wave of frequency $\nu = (E_2 - E_1)/h$ is incident on the material, there is a probability, that this wave will force the atom to undergo the transition from the level 2 to 1. In this case, the photon of energy $E_2 - E_1$ is emitted additionally to the incident one. This process is called stimulated emission Figure 2.9. In the case of spontaneous emission

the phase and direction of the emitted wave is random, while by stimulated emission, the emission of any atoms is in phase to the incoming wave and has the same direction [40].

Flashlamp pumped Nd:YAG lasers are preferred for most LIBS applications, because they provide a reliable and easy to use source of laser pulses of high focused power density. Moreover, the fundamental 1064 nm wavelength can be easily shifted to generate pulses in VIS or UV spectral regions [2, 41]. Moreover, compact Nd:YAG lasers are commercially available in a portable instrumentation. For this reason only solid-state Nd:YAG laser will be described in this chapter.

The typical solid-state laser is built as a resonator, contains an active medium (rod), usually cooled with water and located between two mirrors, one of them (outcopling mirror) is partially transmissive for a laser wavelength, and a pumping source (Figure 2.10). By pumping the inversion population in active medium is created, through radiated spontaneous decay some photons reach the mirrors and reflected back to the rod, where they cause stimulated emission.

The rod is fabricated from Nd^{3+} doped yttrium aluminum garnet (YAG) (Figure 2.11a). YAG hosts are widely used due to its strength, hardness, isotropy and high thermal conductivity. Moreover, the YAG structure is stable in the wide range of temperatures up to the melting point and no phase transformations have been obtained and reported. Nd^{3+} is a four-level gain medium, offering the stimulated emission at 946, 1064, 1123 and 1319 nm. Radiation at these wavelength results from $^4F_{3/2}$ to $^4I_{9/2}$, $^4I_{11/2}$ and $^4F_{13/2}$ respectively (Figure 2.11b). The $^4I_{11/2}$ level depopulates slowly. The lifetime of it is around 230 µs. Therefore, the most common emission wavelength used is 1064 nm [42].

Flashlamps or diodes selectively pump the active medium to achieve the population inversion. The inner surface of pump cavity is coated with high reflectance or scattering material. Nd:YAG lasers are typically pumped with

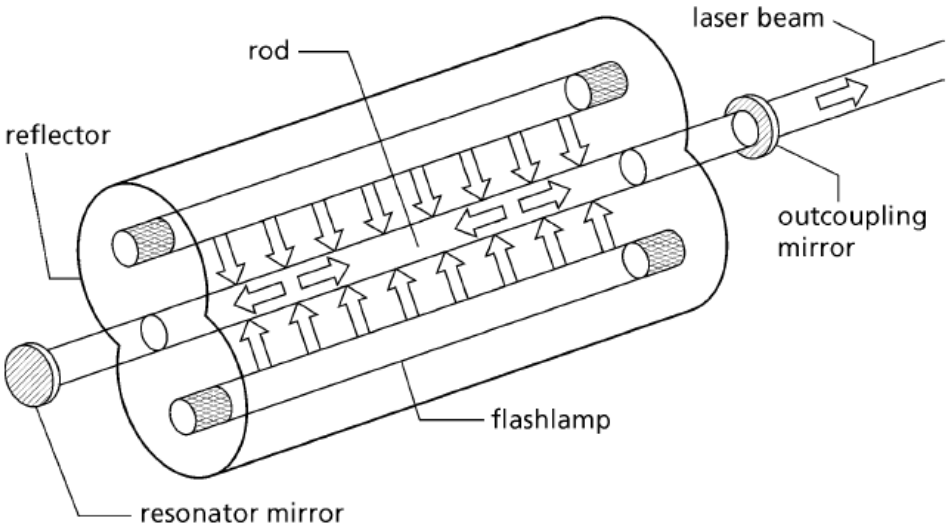

Figure 2.10: Principle setup of a flashlamp-pumped solid-state laser [4]

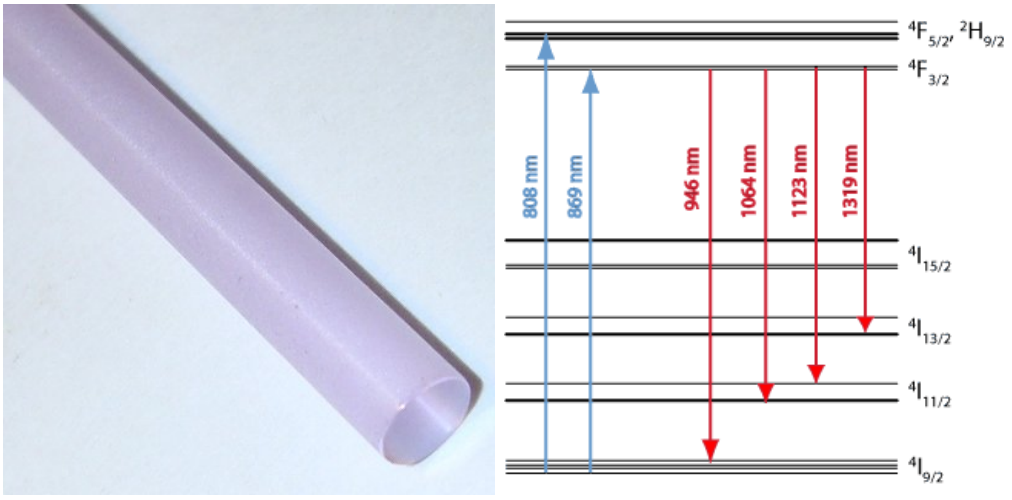

(a) **(b)**

Figure 2.11: a: Image of a Nd:YAG rod (Wikipedia). b: Transitions in Nd^{3+} ion (RP Photonics Encyclopedia).

the Xe or Kr flashlamps, but also the diodes are used. The average lifetime of a Xe flashlamp is around 20-50 million flashes [4]. Diode lasers have smaller dimensions, better pulse to pulse reproducibility and beam quality factor, whereas flashlamp-pumped lasers have the lower cost [43].

To obtain a high energy short pulse the Q-switched (quality switched) system is used. It is achieved by lowering the quality factor Q (ratio of the energy stored in the cavity to the energy loss per cycle). It is implemented by putting an attenuator in the laser cavity. In the Nd:YAG it is realized by using a polariser, a pockels-cell and a waveplate (Figure 2.12). The attenuator blocks the beam path in cavity, inhibiting stimulated emission. By opening the Q-switch in the moment, when the population inversion is maximal, high energy short ns pulses are generated.

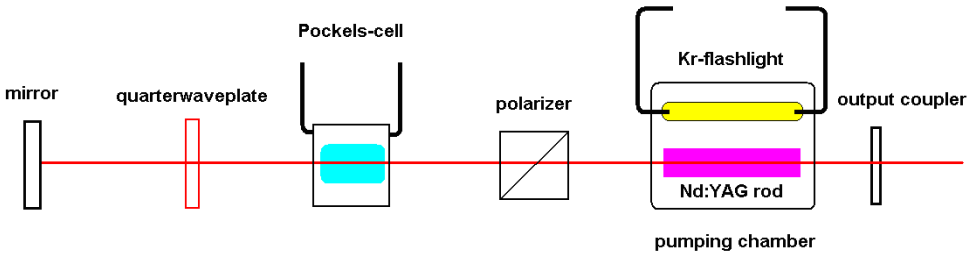

Figure 2.12: Schematic setup of Q-switched Nd:YAG laser, where the Q-switch is realized by pockels cell, polarizer and waveplate located in the cavity [44].

The fundamental 1064 nm wavelength of Nd:YAG can be converted to shorter wavelengths: 532, 354.7 and 266 nm through the second, third and fourth harmonic generation process respectively. The phenomena of harmonic generation was firstly obtained in quartz [41]. For these nonlinear optical crystals such as beta-barium borate (BBO) and potassium dihydrogen phosphate (KDP) are used. In this process an electron is excited to virtual level by two (or more for higher harmonics) photon absorption (Figure 2.13a), then by the

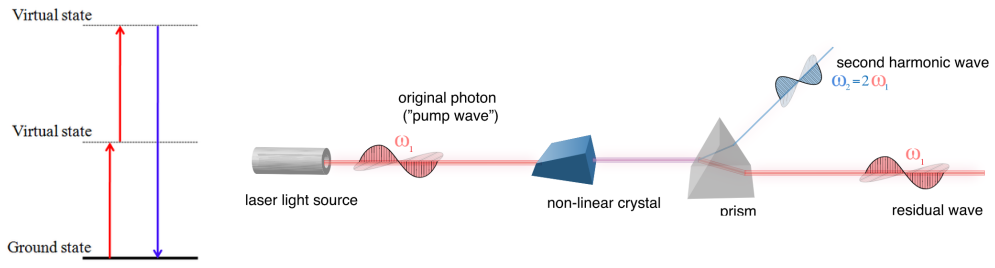

(a) **(b)**

Figure 2.13: a: Energy scheme for SHG process. b: A SHG setup scheme . (Wikipedia).

radiative decay one photon with double frequency and half the wavelength is emitted. The harmonic generation setup is presented in Figure 2.13b.

2.2.2 Spectrometer

LIBS is based on the collection and analysis of an emission spectrum. The important properties of the detecting system are the resolution (minimum wavelength separation at which two spectral features can be observed as single lines) and the width of spectrum. The choice of the exact device depends on the problem to be solved. For example, wider spectral window is needed to monitor the combination of elements simultaneously. Figure 2.14 demonstrates the importance of high resolution detection system.

Some examples of different devices for the spectral resolution used in LIBS are presented below [5]:

- Spectral filters.
  Color filters are used to transmit only the region of interest and reduce intensity of other wavelengths. A notch filter transmits over a broad spectrum, but filters within a small band. It can be used in LIBS to filter the scattered laser light of certain wavelength. Bandpass filters transmit only selected spectral region and have high attenuation in the

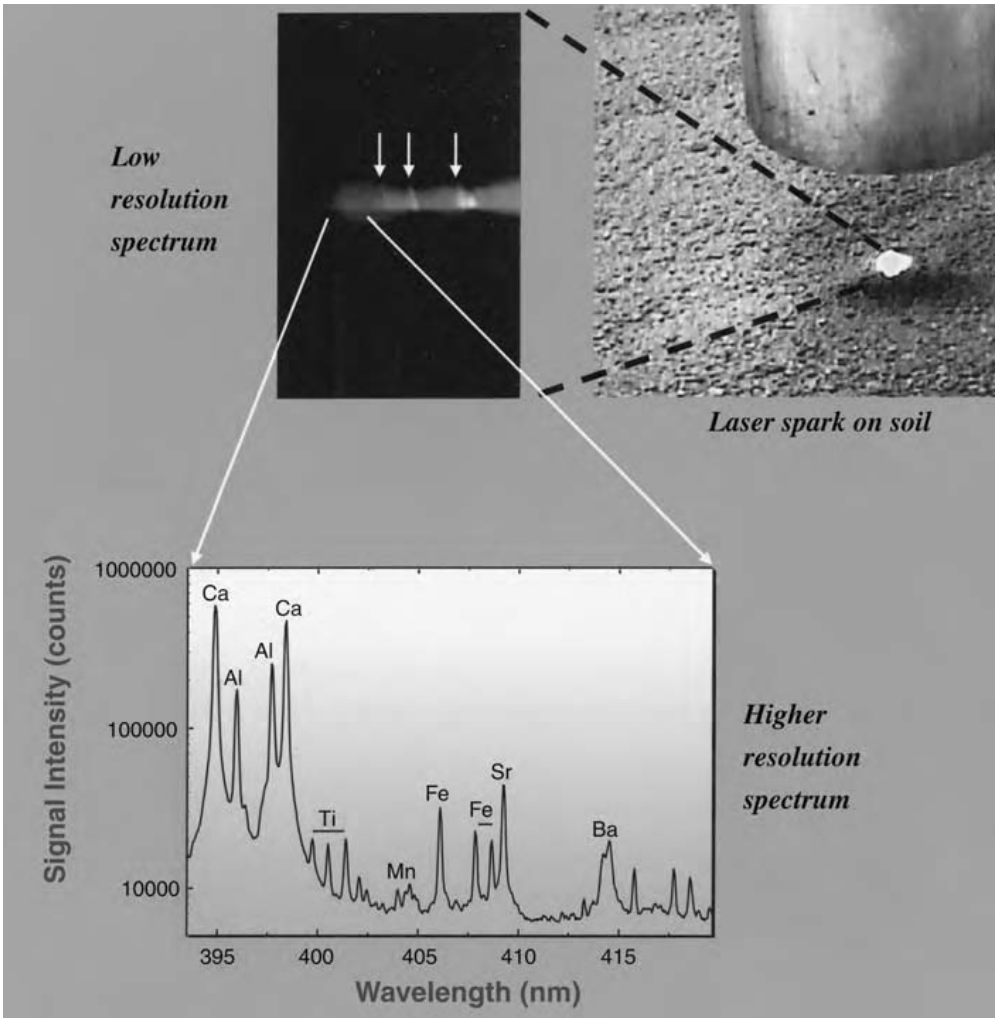

Figure 2.14: Comparison of low resolution LIBS spectrum from the plasma formed on the soil produced by a simple transmission diffraction grating (top) with high resolution spectrum (bottom). On the top spectrum only the strong lines of nitrogen from air are observed whereas the down spectrum presents the emission lines from major and minor elements [2].

rest area. Narrow bandpass filters (< 1 nm) pass a certain emission line and are used in a LIBS setup for monitoring single emission line. Such filters are fabricated using a transmissive for a certain wavelength substrate coated with the combination of dielectrics [2].

- A monochromator is an art of spectrometer used to monitor a single wavelength.

- Spectrometer

  A spectrometer disperses the emitted radiation of plasma to get a spectrum (intensity as function of the wavelength).

  The most often used in LIBS types of spectrometers are Czerny-Turner [7, 14–16, 45, 46] and echelle [18, 19, 47–49]. The schematic image of a Czerny-Turner spectrometer setup is presented on the Figure 2.15. The incoming light passes the entrance slit and then is collimated by a concave mirror and directed onto a grating, where the light is dispersed. The dispersed radiation is focused by a second mirror onto a detector plane [4]. The possible detectors will be discussed later.

  A diffraction grating consist of the large number of equally spaced grooves Figure 2.16. Collimated light hits the grating and is reflected from the periodic structure formed by grooves. This structure behaves as large number of coherent sources. For any wavelength the reflected light can interference constructively and destructively at the certain angles.

  The positive interference condition is described by the equation:

$$d_g(sin\alpha + sin\beta) = n\lambda \tag{2.11}$$

  where d_g is the grating period, α is the angle of incident (negative if the incident beam is on the opposite side to the grating normal respecting

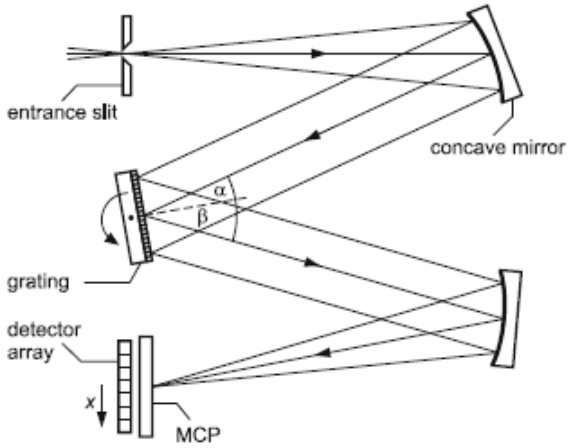

Figure 2.15: Schematic image of a Czerny-Turner spectrometer setup [4]. α is the angle of incident, β is the diffraction angle, MCP - microchannel plate.

to diffracted beam), β is the diffraction angle, n is diffraction order and λ is the wavelength [25]. For a given diffraction order n and angle of incidence α, different wavelengths λ will be diffracted ar different angles λ, what allows the separation of incident polychromatic radiation into its wavelength.

The resolving power of the grating is the product of the diffraction order n and number of grooves N, what incident radiation intercepted:

$$\frac{\lambda}{\Delta\lambda} = nN \tag{2.12}$$

The efficiency of a grating (percentage of incident radiation that is diffracted into desired order) depends on the groove shape, the angle of incidence and the reflectance of the grating coating. One of the parameters influences the efficiency is a blaze angle, what is the angle between the grooves longer side and the plane of the grating. By changing this parameter, the diffracted radiation is concentrated to a specific

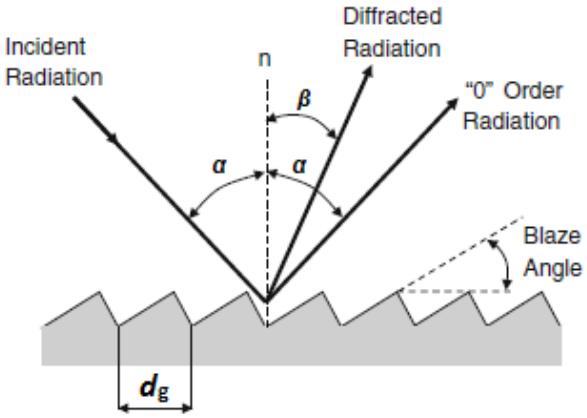

Figure 2.16: Schematic image of a diffraction grating. d_g is the grating period, α is the angle of incident, β is the diffraction angle, n is diffraction order and λ is the wavelength [43].

part of the spectrum, what improves the efficiency of the grating in this region [43].

The Czerny-Turner spectrograph is the most often used spectral resolution device in LIBS. It has high resolution and compact dimension, however, only 10-30 nm spectral window can be detected simultaneously [4].

Much broader spectral range can be dispersed by the echelle spectrograph (200 up to 1000 nm). The setup and beam path of the echelle spectrograph are presented in Figure 2.17. It employs two dispersion elements: a grating and a prism. The incoming radiation entrance the slit, the light is collimated by a mirror and directed into the prism. The refracted light then hits the dispersion grating, where it is dispersed as explained previously. The echelle grating has a low groove density around 80 grooves/mm. The prism with its dispersion at right angle, separates the diffraction orders n and generates two dimensional plot of wavelength λ vs. order n (Figure 2.18a). The prism is used to avoid the overlapping of longer wavelengths of a given diffraction order with

shorter wavelengths of the next one. The example of an echellogramm is shown in Figure 2.18b [4, 5, 43]. All this spectral resolution methods are used depending on the problem to be solved. To choose the most suitable method next questions should be answered:

- What elements are presented in the sample?
- Where their emission lines are located?
- Should all elements be monitored simultaneously?
- How many emission lines do these elements have?

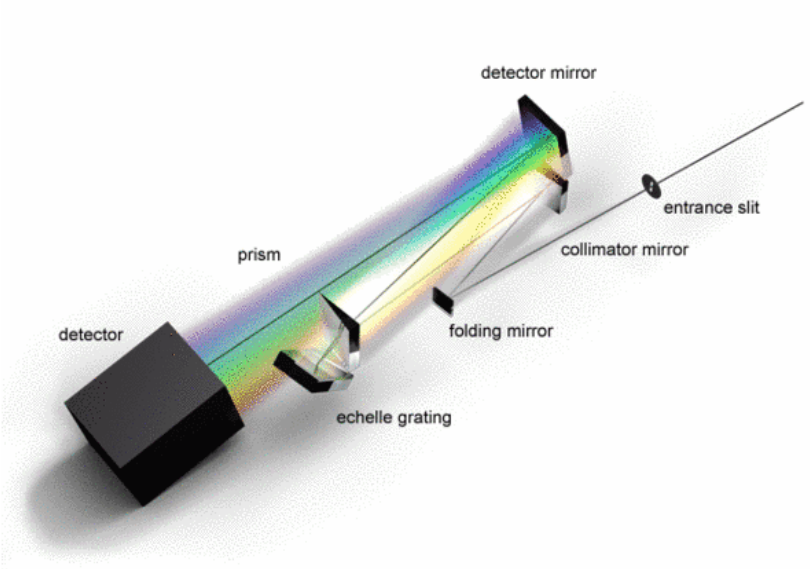

(a)

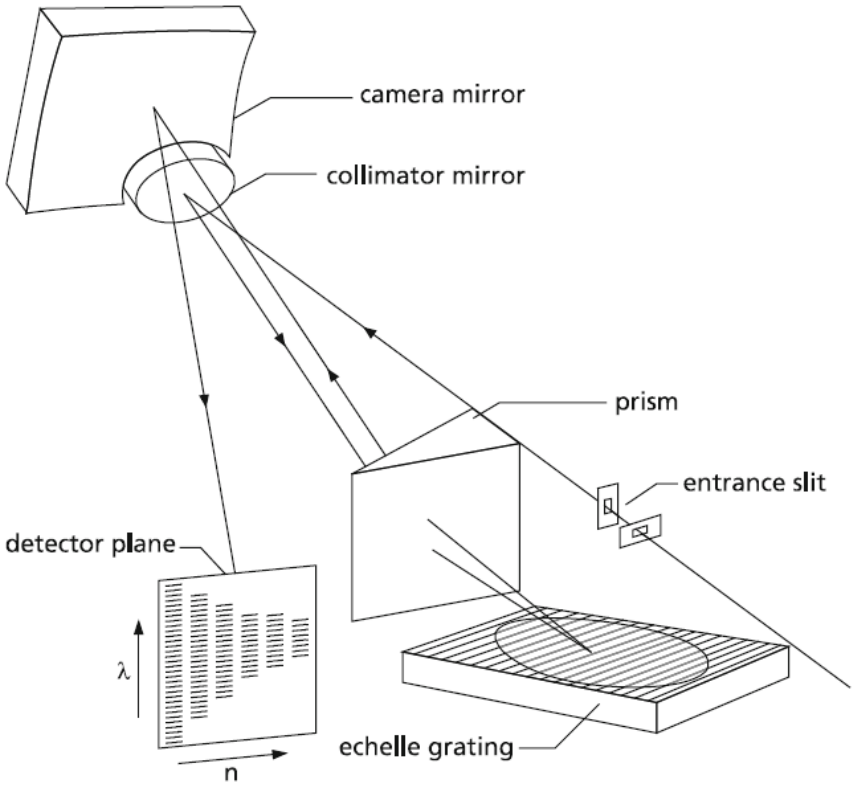

(b)

Figure 2.17: a: Schematic image of an echelle spectrometer optical setup (Lasertechnik Berlin). b: Schematic image of a beam path in an echelle spectrometer [4].

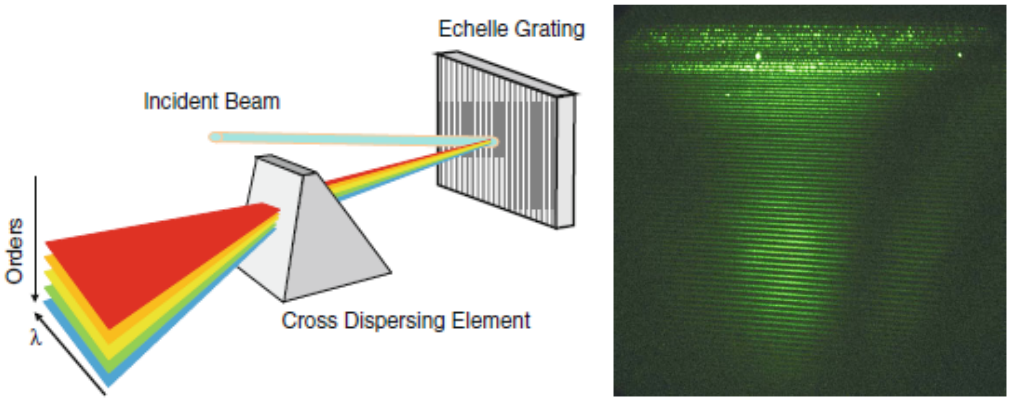

(a) (b)

Figure 2.18: a: Two dispersion elements of an echelle spectrometer: a grating and a prism. b: Echellogramm of the light emitted by a deuterium-tungsten lamp [43].

2.2.3 Detector

A detector choice depends on the spectral resolution methods used. Basically, all detectors can be divided into two groups: time resolved high-speed detectors that can provide a temporal history of the light incident on the device to subnanosecond resolution and light-integrating devices.

The first group is represented by photomultiplier tubes (PMT) and photodiodes (PD), consisting of a photosensitive material that generates a signal proportional to the amount of incident light. This detectors can be used to monitor the plasma evolution as function of time or the elemental emission in combination with the spectral filter or monochromator.

Photodiode arrays (PDA), charge-coupled devices (CCD) and intensified charge-coupled devices (ICCD) are the detectors of the second group. They collect incident light for a period of time and then the charge is read out [43]. CCD detectors consist of an array of single photosensitive elements. When a CCD is exposed to light, each of biased discrete devices (pixels) fabricated on a silicon chip stores charge at the semiconductor-oxide interface. The charge stored by each pixels is a measure of the intensity of irradiated light. Then the scanning and readout is performed by charge transfer along each pixel row of such a device [50].

ICCD is a widely used detector for the LIBS-measurements. The setup of an iCCD is presented in Figure 2.19b. In the ICCD a CCD is combined with a microchannel plate (MCP). The MCP is a thin disk, consisting of many small channel, each serving as an independent electron multiplier. The irradiated photons (dispersed by a spectrometer) generate free electrons at the photocathode. An electric field is applied to accelerate the electrons toward the MCP. The electrons hitting the MCP channels wall produce secondary electrons and this process is repeated many time. By this the signal is intensified. Further, the electrons are accelerated into a phosphor screen, that reconverts it to the light. By a fiber optical plate the light is transported

to the CCD [4]. Moreover, the MCP acts as fast electronic shutter to block and transmit the spectral images from the spectrograph to the CCD-chip. The gating is crucially important for LIBS, because it allows to detect in the time range, when the bound-bound transitions take place and characteristic elemental peaks can be obtained.

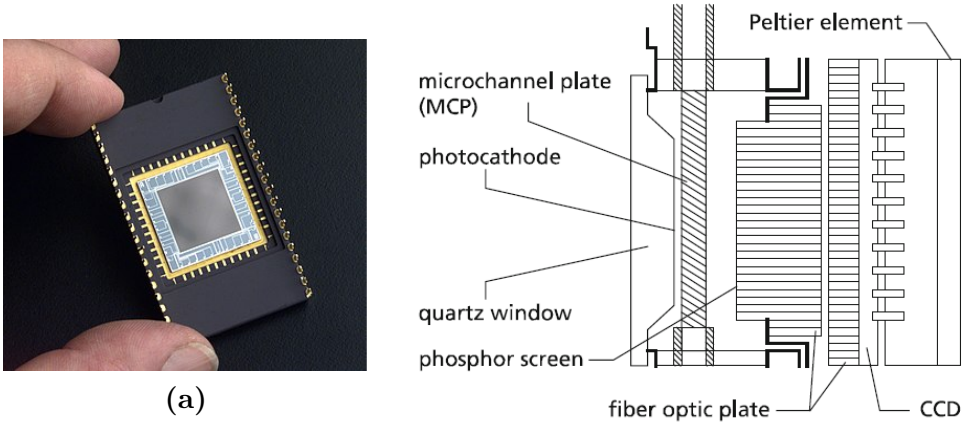

Figure 2.19: a: CCD (Wikipedia). b: Schematic image of ICCD [4].

In this section the components for LIBS-setup were described and the state-of-art devices were listed. A LIBS setup can be constructed for each application, though a combination of Nd:YAG laser combined with an echelle-spectrograph and an ICCD camera offers the possibility to analyse almost all material, due to high energy pulses of laser, wide spectral window of the spectrometer and high sensitivity of ICCD camera. Moreover, many elements can be detected simultaneously.

2.3 Depth profiling methods

Quality control of plated coating is of substantial important. In this chapter the industrial methods used to control the thickness, chemical composition and homogeneity of plated layer will are listed and discussed.

X-ray fluorescence (XRF) is one of the most common methods of compositional analysis used for measuring electroplated alloy composition and thickness. In this method X-rays produced by an X-ray tube hit a deposit and ejects an electron from the inner orbital of the atom. The electron structure of the atom becomes unstable and an electron from the higher level falls into the lower orbital Figure 2.20. The energy difference is released in the form of a photon. Emissions is specific for each element and the intensity is proportional to coatings thickness. The system may be calibrated with a known thickness and composition standard for additional accuracy. X-ray fluorescence works well for the analysis of heavy elements like metals in quantities above 0.5 % and makes the thickness analysis in the range 0.25 - 10 µm possible. XRF is a non-destructive method and can be applied for many different plating applications [51].

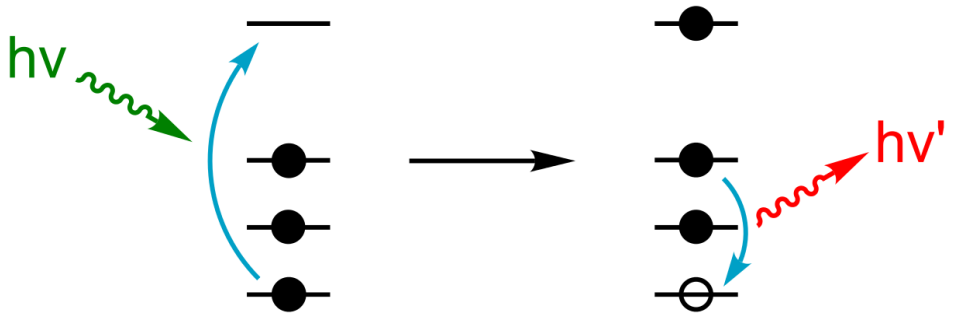

Figure 2.20: Schematic image of X-Ray fluorescence process (Wikipedia)

.

The glow discharge optical emission spectrometry (GD-OES) represents a rapid depth-profiling technique capable of qualitative and quantitative ele-

mental analysis of layered samples in the thickness range 1 nm - 100 µm. In this method the sample atoms are sputtered in the glow discharge cell under the voltage 600-1500 V in the argon atmosphere. After that, they are excited by plasma species and emit characteristic light. This method has very good sensitivity for a wide range of elements including light elements, detection limits in the range of 0,0001–0,01% mass fraction. The very limited lateral resolution is determined by the anode inner diameter, typically 2mm for existing commercial systems. Smaller anodes of 1 mm are available, but at the cost of poor depth resolution and sensitivity. Moreover, a flat sample is required in standard configuration, special adapters for curved and cylindrical surfaces are available but with restrictions on minimum size to several mm width [52, 53].

Energy dispersive X-ray spectroscopy (EDX) is a conventional technique for elemental analysis after coating production. This technique provides excellent lateral resolution (few microns) but suffers from low sensitivity for light elements analysis [7]. Moreover, for depth profiling preparation of cross-sections is needed, what is very time consuming.

LIBS used for depth profiling in this work requires no sample preparation, no shape restrictions, no vacuum. A further advantage of LIBS is the possibility to analyze almost all elements, including light, what is not possible using EDX-spectroscopy.

Chapter 3

Experimental

3.1 Samples

To investigate the wavelength-dependend behaviour of the metal coatings industrial samples such as galvanic copper and nickel on steel and electroless nickel containing 2-4 wt% phosphorus (NiP) on steel with different thickness were used. All samples used for this work were produced by Happy Plating GmbH. The thickness and the homogeneity of the sample was determined by scanning electron microscopy (SEM) and EDX spectroscopy on the cross-sections.

Preparation of cross-sections

A small piece of each sample has been cross-cut and placed into a mounting cylinder of a hot mounting press (Struers CitoPress-1) and carbon resin was added. A temperature of around 180° C and a pressure of about 250 bar was applied during the embedding of the specimen. Than, the embedded sample was ground with a grinding machine (Struers LaboPol-25) using silicon carbid (SiC) paper of different grit size and finally polished with MD-Mol and MD-Nap textiles (produced by Struers GmbH). All steps of the grinding and

Table 3.1: Polishing parameters for the preparation of cross-sections for electron microscopy and EDX-spectroscopy

Step	Polishing agent	Rotation [rpm]	Additive	Time [s]
1	SiC 800	150	water	
2	SiC 1200	150	water	20
3	SiC 2500	150	water	30
4	SiC 4000	150	water	90
5	MD-Mol 3μm	150	abrasive paste green	180
6	MD-Nap 0.04μm	130	water	120-240

polishing are presented in Table 3.1. After each step the cross-sections were rinsed with distilled water. The result of polishing was controlled via optical microscopy.

Thickness measurements

The thickness of the coatings were determined via scanning electron microscopy (SEM) and energy dispersive X-ray spectroscopy. Therefore, scanning electron microscope Zeiss Supra 55 VP was used. High-energy electron (20keV) backscattered electron images were taken to proof homogeneity and sticking of the layers to steel substrate and determine the sites for EDX measurements. Thickness was also measured from BSE images in SmartTiff program.

EDX line-scans with 15 points each were taken 9 times at the different sites perpendicularly across the layer. Resulting data points of all scans were combined into one plot. The EDX-system was not calibrated to measure quantitative respective elements,for this reason resulted values of atomic weight fracture are not trustworthy. Though, the qualitative presence of each element was obtained. To calculate the exact thickness of layers, sigmoid fits based on the complementary error function of depth under the surface

d $\mathrm{erfc}(d) = 1 - \mathrm{erf}(d) = \frac{2}{\sqrt{\pi}} \int_d^\infty e^{-t^2}\, dt$ was used, where the centroid was identified as layer thickness.

3.2 Setup

The setup used for LIBS-measurements is presented in Figure 3.1 and Figure 3.2. This setup allows to carry out the experiments at two wavelength: 532 and 1064 nm. It consist of SpectraPhysics GCR-130 Nd:YAG laser, which will be described thoroughly in the next subsection, focused by 2 in. fused silica focusing lens on a sample mounted on a micrometer positioning stage (PI M-403.625) with NI Mercury Step C-66 stepper motor controller. The focus position z was adjusted by a micrometer screw.

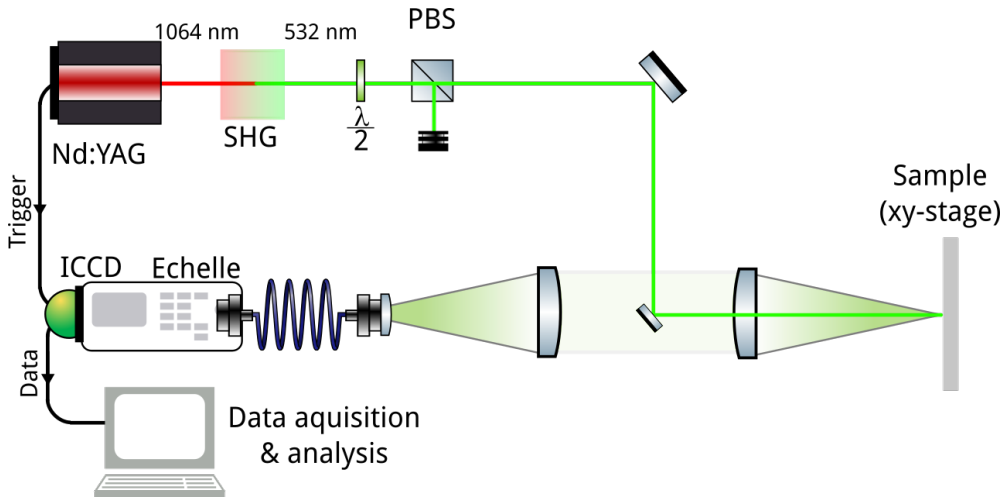

Figure 3.1: LIBS-stratigraphy setup. SHG = second harmonic generator, $\frac{\lambda}{2}$ = wave-plate, PBS = polarising beam splitter.

The light emerging from the recombination processes in the plasma after the black body radiation ceases to be dominant (shutter delay 0.4 µ s relative to the laser pulse trigger) has been collected by the same lens and then refocused with an analogue 2 in. lens into a glass fiber connected to an Echelle spectrograph (Aryelle 200, Laser Technik Berlin GmbH). Between

two lenses a 1/2 in. dichroic mirror was placed to adjust the laser beam path and allow the plasma light detection. The light spectrum is projected onto an intensified charge-coupled device (ICCD) camera (ICCD 734, Gen. II, Andor). Before each CCD readout, a dark image was taken and substracted automatically to eliminate the noise originating from thermal background. The sample was subdivided into grids of 25 spots containing 100 laser pulses.

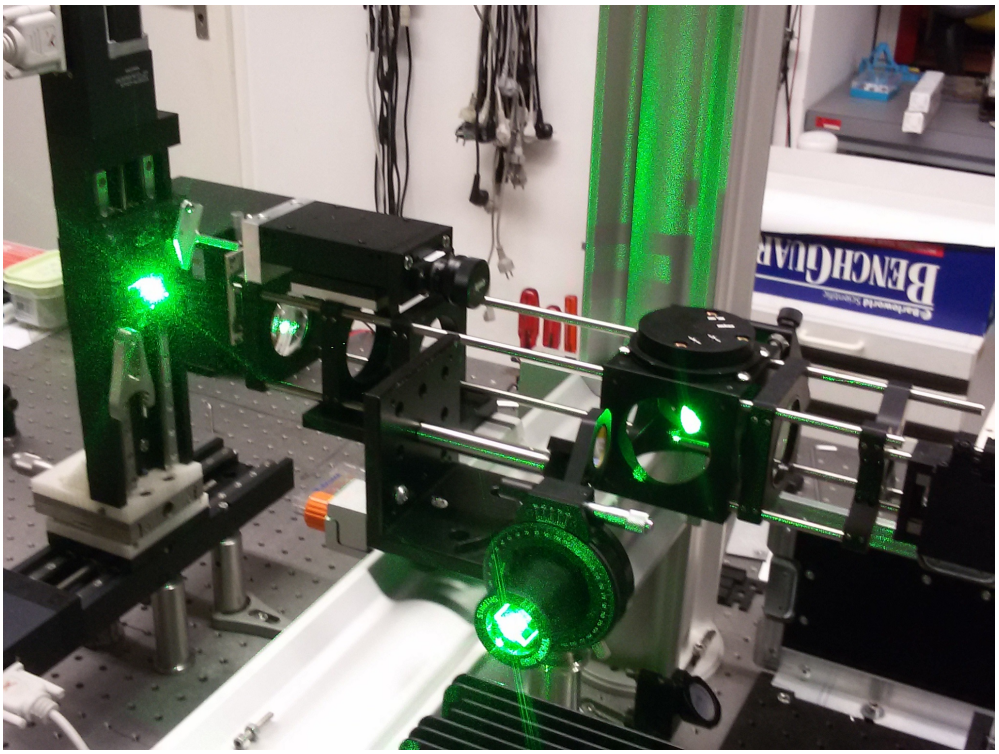

Figure 3.2: A photographic image of the LIBS-setup

The recorded spectra of those spots have been averaged in order to improve signal-to-noise ratio (SNR). The distance between the spots has been 5 mm. The spectra have been recorded at a laser repetition rate of 0.5 Hz, which is the ICCD-camera's readout limit.

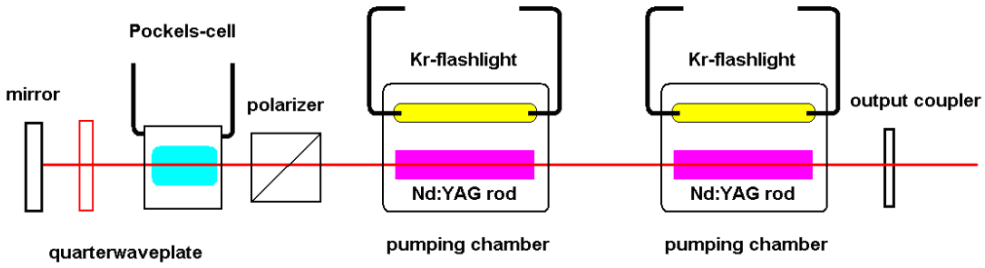

Figure 3.3: Schematic image of the SpectraPhysics GCR-130 Nd:YAG Laser

Laser

A SpectraPhysics GCR-130 Nd:YAG laser, which produces 7 ns pulses at 1064 nm and has a repetition frequency 20 kHz, was used. The laser consists of two Nd:YAG rods, pumped with Kr-flashlights, located in gold plated chambers (Figure 3.3). A pulse generation is achieved through Q-switching, what is realised by Pockels cell, combined with polarizer and waveplate. The resulting maximum output power is 6 W.

A harmonic generator consisting of β-barium borate (β-BBO) crystal in argon-purged heated chamber was used to double the frequency of output light and produces 5 ns pulses at 532 nm. To adjust the energy Thorlabs polarising beam splitter (PBS) combined with half-wave plate was used and the energy was measured using pyroelectric power meter (Ophir Photonics). The limit of spectra acquisition of the spectrometer is 0.5 Hz, due to this the frequency of laser was adjusted at 0.5 Hz by sending a signal to the flash lamps and Q-switch control unit, forcing them to switch in 0.5 Hz rhythm. The energy was measured and adjusted at 20 Hz. It was found, that the laser energy drops with the lower repetition frequencies (around 4 times). The dependency of pulse energy to laser power is presented in Figure 3.4. The

slope of the graph gives the calculation coefficient 0.013 for frequencies lower than 10 Hz.

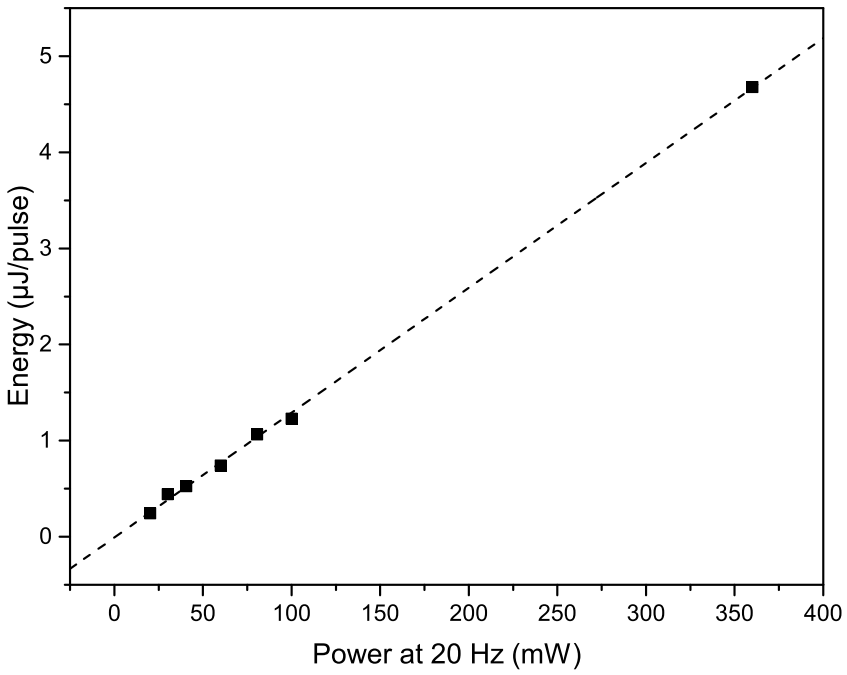

Figure 3.4: Dependency of laser pulse energy to the laser power at the frequencies lower then 10 Hz. The dash line presents the linear fit to measured data, slope of the line gives the calculation coefficient and is equal 0.013.

3.3 Beam diagnostic

The knowledge of laser beam parameters are of substantial importance for investigation of ablation behaviour. In this subsection important parameters and their determination are discussed.

3.3.1 Focus position determination

The focus position was determined by ablation of the thermosensitive paper. Another opportunity would be a film of a black lack on a glass substrate. An important criteria for material choice is the high absorptivity of the laser light. The power of the laser beam was adjusted at 10 mW. The focus position was varied by the change of the distance between the focusing lens and the sample surface. For each focus position z 5 laser pulses were done. The squares of the ablation craters were measured with Olympus STM-MJS optical microscope (Figure 3.5 b) , then diameters were calculated and plotted related to stage position and minimum of parabolic fit gave the focus position (Figure 3.5 a).

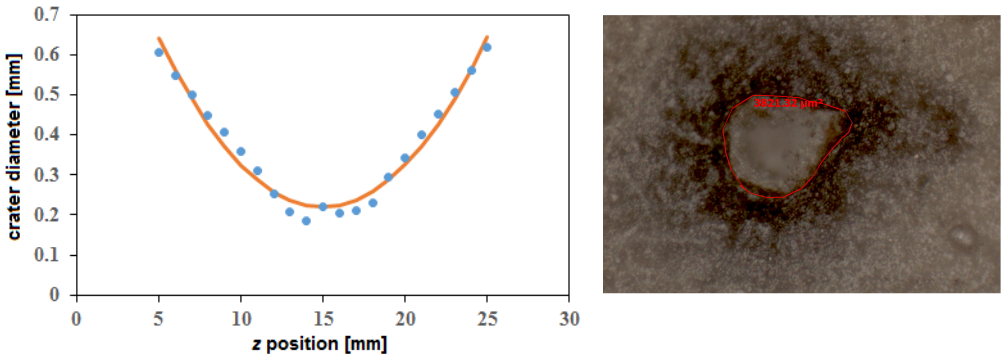

(a) (b)

Figure 3.5: a: An example of the focus determination. The line represents the parabolic fit to the measured data. The minimum of the parabolic fit gives the focus position (z_0 = 15 mm). b: An optical microscopy image of the ablation crater on the thermosensitive paper. The red line represents the measurement of the crater square.

3.3.2 Beam profiling

The most important parameters for the laser beam quality characterisation

For the investigation of the ablation properties of the material, the knowledge of the laser beam propagation parameters is of substantial importance. In this section the key laser beam parameters and the determination methods used in this work are described.

Nd:YAG laser provides the Gaussian beam, where the transverse profile of the beam's electric field distribution of ground transversal electromagnetic mode TEM_{00} can be described with a Gaussian function:

$$I(x,y) = I_{\max} \exp \frac{-2r^2}{w^2} = I_{\max} \exp \frac{-8(x^2+y^2)}{d^2} \tag{3.1}$$

where x-y plane is perpendicular to propagation direction z and $z = \sqrt{x^2+y^2}$ is radial coordinate. A beam diameter d increases with the distance z from a beam waist as described in

$$d(z) = d_0 \sqrt{1 + \left(\frac{z}{z_{\mathrm{R}}}\right)^2} \tag{3.2}$$

where z_{R} is Rayleigh length, what is the distance along the propagation direction of a beam from the waist to the place where the area of the cross section is doubled, or beam radius increased by a factor $\sqrt{2}$. Doubled z_{R} gives depth of focus (DOF).

In far field $z \gg z_{\mathrm{R}}$ beam radius increases linearly with z and gives beam divergence θ.

$$\theta = \frac{d_0}{z_{\mathrm{R}}} = \frac{4\lambda}{\pi \cdot d_0} \tag{3.3}$$

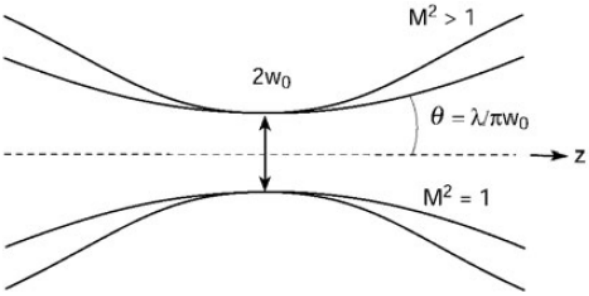

Figure 3.6: Propagation of an ideal Gaussian laser beam with $M^2 = 1$ compared to a laser beam with $M^2 > 1$ with the same diameter $d_0 = 2\omega_0$ [54].

For the ground mode TEM_{00} beam parameter product can be calculated from d_0 and θ.

$$\frac{d_0 \cdot \theta}{4} = \frac{\lambda}{\pi} \tag{3.4}$$

At higher transversal modes or mix of modes both d_0 and θ times factor M higher than at TEM_{00}. In this case the beam parameter product:

$$\frac{d_0 \cdot \theta}{4} = M^2 \frac{\lambda}{\pi} \tag{3.5}$$

where beam quality factor M^2 represents the degree of variation of a beam from an ideal Gauss beam (TEM_{00}). It reflects how well a laser beam can be focused to a small spot, or how well a divergent laser source can be collimated. In Figure 3.6 the schematic image of propagation of a Gaussian TEM_{00} beam ($M^2 = 1$) is compared with the same laser beam but with $M^2 > 1$. The beam with lower M^2 has lower beam diameter and divergency. For the M^2 calculation the knowledge of beam radius is necessary. It was determined by a combination of the two pathways: "cutting edge" and "squared diameters" (D^2) method.

Gaussian beam radius/diameter measurements using "cutting edge" method

A razor blade was scanned through the beam in x and y direction as schematically presented on the Figure 3.7 and transmitted energy as a function of razor blade position (x' and y') was measured using a pyroelectric powermeter. The same procedure was repeated for different z-positions. To calculate the transmission of beam with power P dependent to razor blade position x' the integral was used:

$$T(x') = \frac{1}{P}\int_{x'}^{+\infty}\int_{-\infty}^{+\infty} I(x,y)dxdy = \sqrt{\frac{2}{\pi}}\frac{2}{d}\int_{x'}^{+\infty}\exp\frac{-8x^2}{d^2}dx = \frac{1}{2}\left[\mathrm{erf}2\sqrt{2}\frac{x}{d}+1\right] \tag{3.6}$$

The beam radius is defined as difference of the positions, where transmission is equal 16% and 84% (Figure 3.8).

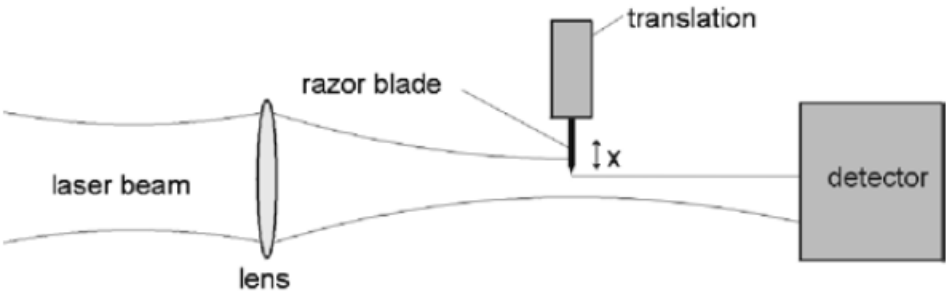

Figure 3.7: Scheme of the "cutting edge" method for the determination of the Gaussian beam radius w_0 and the beam quality parameters [27].

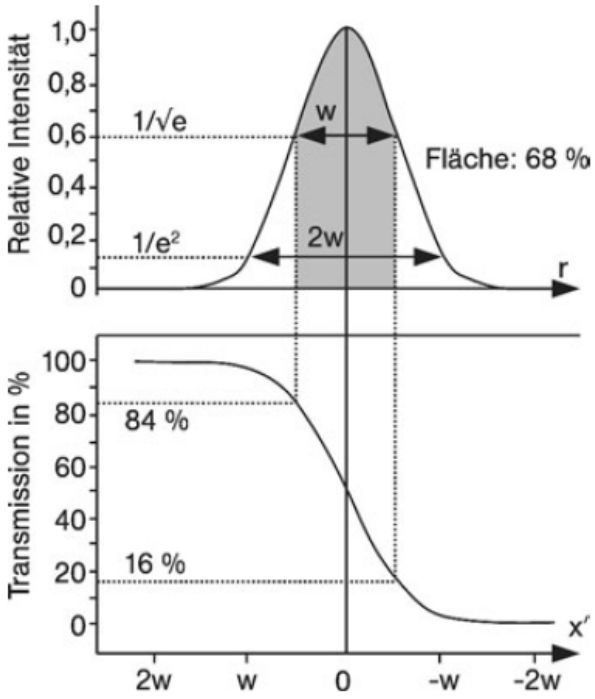

Figure 3.8: Scheme of the "cutting edge" method for the determination of the Gaussian beam radius. Top: Gaussian intensity distribution of the laser beam. Bottom: Transmission dependent on the position of the razor blade. The Gaussian beam diameter $2w_0$ is defined as the width in the positions where the intensity has fallen to $1/e^2$. [54]

Beam radius/diameter determination via D^2 method

For the measurements of the Gaussian radius in the positions z near to z_0 the Gaussian beam radius was determined with D^2-method ablating the thermosensitive photo-paper. For Gaussian beam profile the relation between the crater diameter D and the maximum laser fluence can be written as:

$$D^2 = 2\omega_0^2 \ln \frac{F}{F_{\text{th}}} \tag{3.7}$$

Equation 3.7 is also valid if the laser fluences F and F_{th} are replaces by pulse energies E and E_{th}:

$$D^2 = 2\omega_0^2 \ln \frac{E}{E_{\text{th}}} \tag{3.8}$$

Taking in account Equation 3.8 Gaussian beam radius w_0 can be obtained from a semi-logarithmic plot of the squared diameters of ablated area D^2 vs pulse energy E. Therefore, the ablation experiments were performed with different laser pulse energies and number of pulses. The squares of the craters were measured with optical microscope Olympus STM-MJS and the diameters were calculated. The slope of the line yields w_0. Moreover, the intercept of the linear fit with the x-axis gives the threshold energy.

Combination of "cutting edge" and D^2 methods

The beam diameter was measured at minimum ten z positions as described in subsubsection 3.3.2. The change of d_0 can be described by following equation:

$$d^2(z) = d_0^2 + (z - z_0)^2\theta^2 \tag{3.9}$$

Near to the focus position the fluence was high enough to ablate the razor blade, for this reason the beam diameter measurements calculated with transmitted energy values near and at focus position are not trustworthy and

were replaced by the values from D^2 measurements on the thermosensitive paper. Beam diameter values $d(z)$ were fitted with second grade polynomial:

$$d^2 = A + Bz + Cz^2 \tag{3.10}$$

The position of beam waist, its diameter and divergence in far field can de determined from coefficient:

$$z_0 = -\frac{B}{2C}, d_0 = \sqrt{A - \frac{B^2}{4C}}, \theta = \sqrt{C} \tag{3.11}$$

With this the beam quality factor was calculated:

$$M^2 = \frac{d_0 \cdot \theta}{4} \cdot \frac{\pi}{\lambda} \tag{3.12}$$

The Figure 3.9 represents the described beam diagnostics method, the calculated values are presented in the Table 3.2.

Table 3.2: Beam parameters determined by the combination of "cutting edge" and D^2 methods

λ [nm]	τ [ns]	w_0 [µm]	z_R [cm]	M^2	θ [rad]
1064	7	75	0.203	8	0.07
532	5	62	0.170	13	0.07

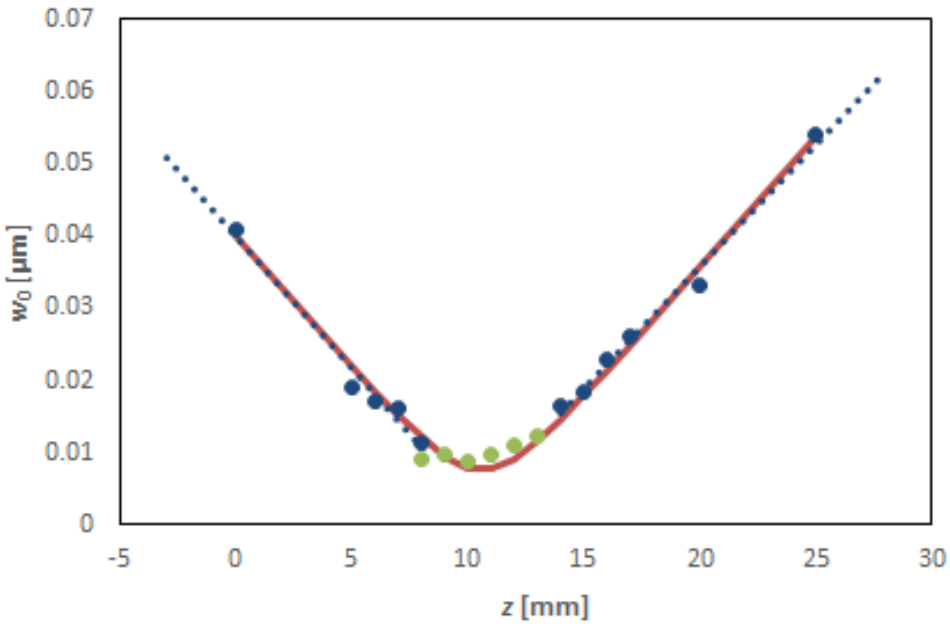

(a): 1064 nm

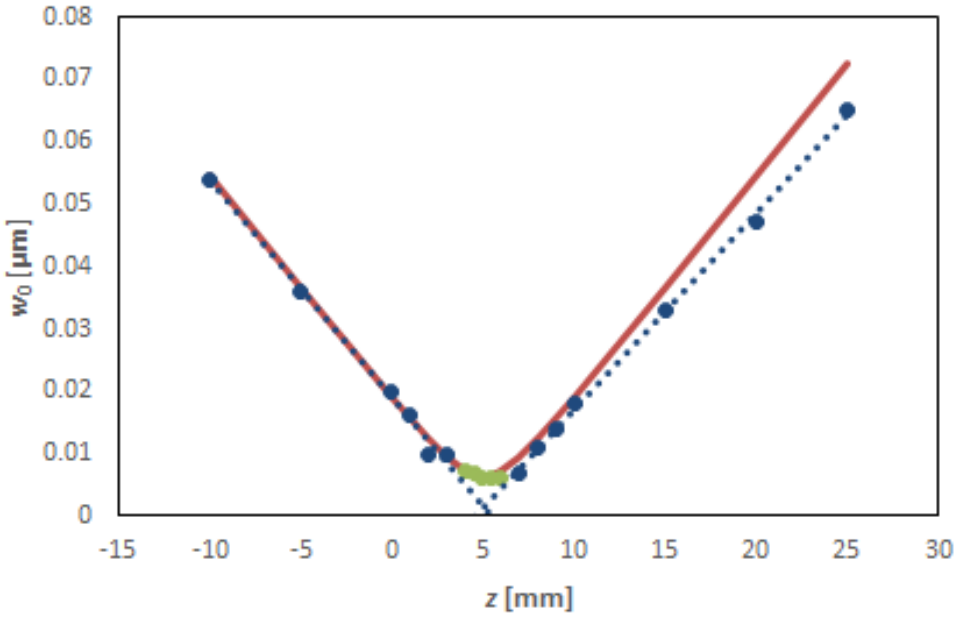

(b): 532 nm

Figure 3.9: Plot representing Beam quality, Gaussian beam radius, Rayleigh length measurement, combining "cutting edge" (blue dots) and D^2 method (green dots). Red lines is the parabolic fit to measured data, where the minimum gives the focus position. The blue dashed line represents linear fit to the data in far field and shows the divergence of the laser beam. The coefficients of fitting equation $d^2 = A + Bz + Cz^2$ are used to calculate z_R, w_0, M^2, θ.

3.4 LIBS-data analysis

3.4.1 Linear correlation

A linear correlation method, based on an using total spectral information to compare a similarity between spectra measured and standard spectra, was applied in this work. In this method, the measured peak intensities are replaced by correlation coefficient r, described by Equation 3.13. The correlation coefficient ranges between -1 (perfect correlation) and +1 (perfect anticorrelation).

$$r = \frac{\sum_{\lambda} \left(I_{\lambda,\mathrm{M}} - \bar{I}_{\mathrm{S}}\right)\left(I_{\lambda,\mathrm{M}} - \bar{I}_{\mathrm{S}}\right)}{\sqrt{\sum_{\lambda} \left(I_{\lambda,\mathrm{M}} - \bar{I}_{\mathrm{M}}\right)^2}\sqrt{\sum_{\lambda} \left(I_{\lambda,\mathrm{S}} - \bar{I}_{\mathrm{S}}\right)^2}} \tag{3.13}$$

The term in the numerator of Equation 3.13 is the covariance of the measured spectral intensity $I_{\lambda,\mathrm{M}}$ and the spectral intensity of the standards' signal $I_{\lambda,\mathrm{S}}$. The factors in the denominator are the variances of each.

The recorded spectra have been Pearson correlated (see Equation 3.13) with a standard spectrum obtained by averaging spectra of a 100 laser pulses on pure element Ni, Cu and Fe bulk metal sheets (standards), respectively. The decay or rise of the correlation coefficient r indicates the breach of the metals' interfaces.

This method can eliminate drawbacks of a classical single emission line intensity evolution method, such as an peak intensity decay due to laser fluence fluctuations, pulse-to-pulse fluctuations in plasma evolution and sample inhomogeneities. It thus give an significant improvement in a quality of depth profiles [6, 18, 19, 44]. Moreover, this method can be used to distinguish the layers having very similar composition [6].

3.4.2 Fitting functions

The exponential rise and decay functions describing behaviour of LIBS depth profiles have been developed in [44]. The Equation 3.14 and Equation 3.15 formulate an empirical fitting function for exponential rise and decay of correlation coefficient, respectively, where $r_j^i(N)$ is correlation coefficient of measured spectrum at pulse number N with the standard spectrum of element i in the layer j, A^i is characteristic amplitude of correlation coefficient, k_j^i represents rise or decay constant, $N_{(j-1,j)}^i$ describes the number of laser pulses needed to achieve the interface between layers, c_j^i is baseline shift. $-aN^2$ is damping term, that describes the decay of the signals with high N due to plasma shielding [38].

$$r_j^i(N) = A^i\left\{1 - \exp\left[-k_j^i(N - N_{j-1,j}^i)\right]\right\} - aN^2 + c_j^i \tag{3.14}$$

$$r_j^i(N) = A^i \exp\left\{1 - \left[\frac{k_j^i + N - N_{(j-1,j)}^i}{k_j^i}\right]^2\right\} - aN^2 + c_j^i \tag{3.15}$$

3.5 Investigation of ablation behaviour: threshold fluence and incubation coeffcicient

To study the ablation and incubation properties of the materials, systematic ablation experiments were performed varying the pulse number and the laser pulse fluence at 20 Hz. A threshold fluence $F_{\text{th}}(N)$ was determined using D^2 method (subsubsection 3.3.2) as an intercept of the semi-logarithmic plot of the squared diameters of the ablated craters D^2 vs the laser fluence F with the x axis. The incubation coefficient was determined according to Equation 2.9 by calculation the slop value in the logarithmic plot of $NF_{\text{th}}(1)$ versus pulse number N and the threshold fluence for 1 pulse $F_{\text{th}}(1)$ were estimated as an intercept with y-axis.

Chapter 4

Results and discussion

4.1 Sample characterisation

For the investigation of the wavelength on the LIBS-stratigraphy plated Ni, Ni-alloys and Cu coatings on steel were chosen (Table 4.1). The quality of the coatings and the thickness were controlled by SEM and EDX-spectroscopy on the cross-sections. Some samples showed the coating detachment as presented in Figure 4.1 and Figure 4.2. The bad adhesion of the plated layers to the steel substrate might be explained by the technological problem during the activation step of the electroplating. This samples were excluded from further measurements.

It is necessary to mention that the samples are inhomogeneous (Figure 4.3a and Figure 4.3b), what can be related to the plating process. For the determination of the thickness the atomic fraction from the EDX-analysis of C, which represents the embedding material, Ni or Cu for a layer and Fe representing steel were plotted versus the position d (Figure 4.3c). This data were fitted using the sigmoid based on the complementary function $\mathrm{erfc}(d) = 1 - \mathrm{erf}(d) = \frac{2}{\sqrt{\pi}} \int_d^\infty e^{-t^2}\, dt$ and the centroid of the function was identified as the layer thickness. The thickness value are presented in the Ta-

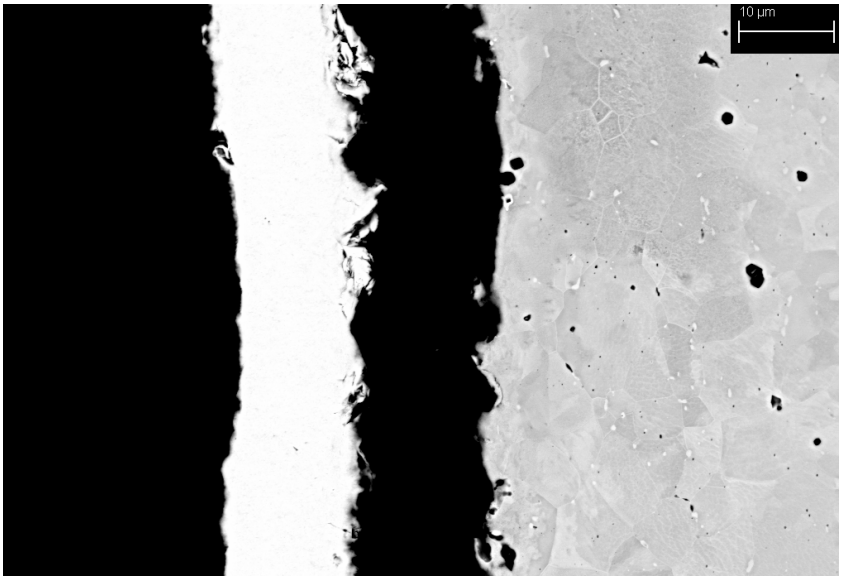

Figure 4.1: BSE image of the Ni sample excluded from the further measurements. The image represents a detachment of coating from the substrate.

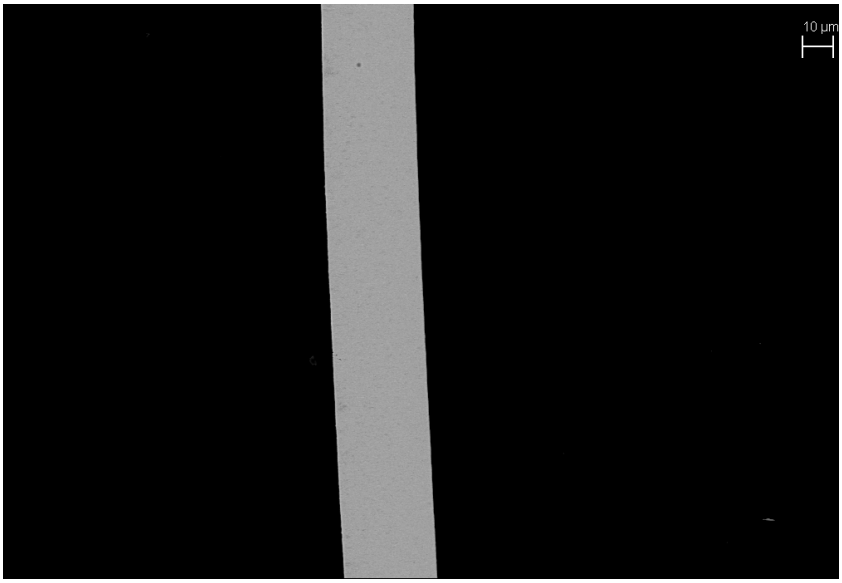

Figure 4.2: SEM image of the Ni layer detached from sample.

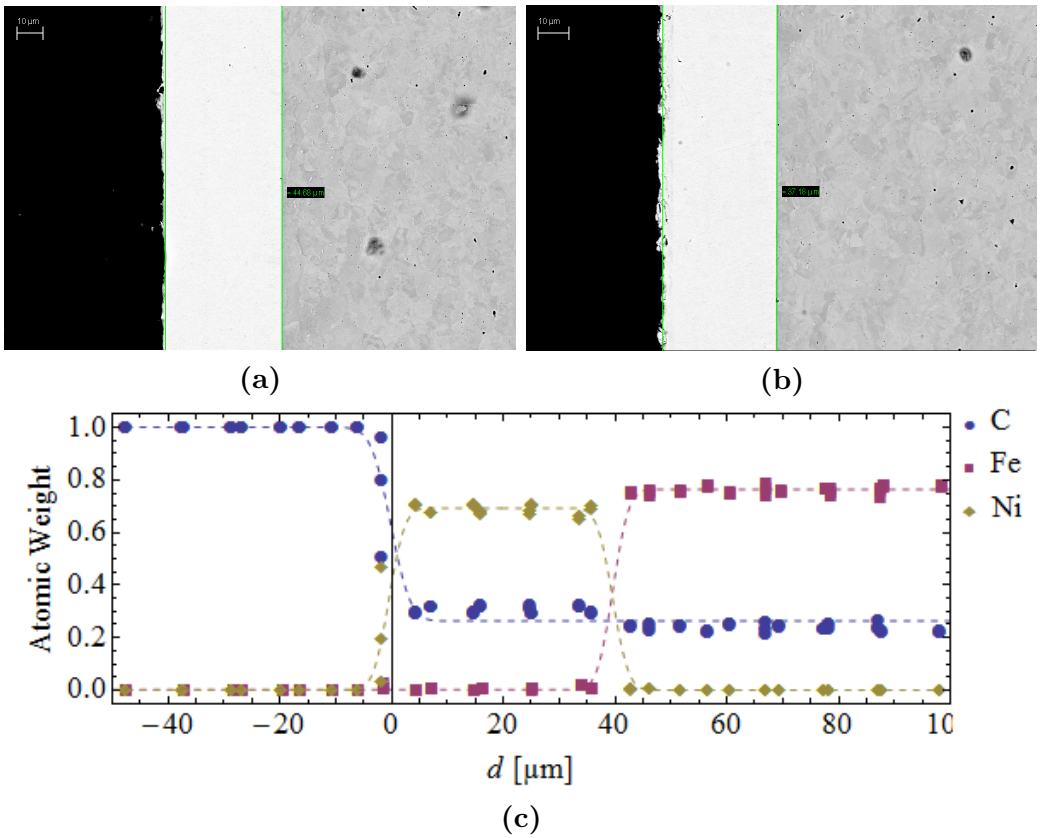

Figure 4.3: BSE image of Ni-3 sample, representing inhomogeneous thickness on the different sites (a, b) and the EDX line scan on the same sites, where the dash lines represent the sigmoid fit (c). The mean values of the centroids for Ni and Fe fit is identified as layer thickness.

Table 4.1: Samples used for this work

Sample ID	Coating material	Thickness [µm]
Ni-1	electroplated Ni	8.0±1.5
Ni-2	electroplated Ni	30.9±11.3
Ni-3	electroplated Ni	40±11.2
NiP-1	electroless plated Ni-P	4.5±0.5
NiP-2	electroless plated Ni-P	11.7±1.5
NiP-3	electroless plated Ni-P	23.1±6.2
Cu-1	electroplated Cu	13.9±2.3
Cu-2	electroplated Cu	17.7±3.5
Cu-3	electroplated Cu	20.7±6.3

ble 4.1. The fitted values (centroid of the sigmoid function) are in the good agreement with BSE measurements results.

4.2 Threshold fluence and incubation coefficient determination

Before starting the LIBS experiments, the ablation and incubation behaviour of the materials was studied. It is necessary to find out the threshold fluence for the sufficient stratigraphy measurements. Therefore, systematic ablation experiments with fluence from 8 to 67 and 6 to 45 J/cm^2 for the laser wavelengths 532 and 1064 nm respectively were performed on each sample. For each fluence and pulse number the experiment was repeated 5 times. The ablation craters were investigated by optical microscopy and the craters square was measured as presented in Figure 4.4 and Figure 4.5. The crater diameters were plotted against laser energy and then the threshold fluence were estimated as an intercept with x axis according to D^2 method (subsubsection 3.3.2). An exemplary graph is presented in Figure 4.6. The full documentation of the threshold fluence and incubation coefficient determination is listed in Appendix A.

The incubation coefficient describing the decrease of threshold fluence with increasing pulse number $F_{\mathrm{th}}(N) = F_{\mathrm{th}}(1)^{\xi-1}$ was determined by calculation the slop value in the logarithmic plot of threshold fluence $F_{\mathrm{th}}(N)$ versus pulse number as presented on the Figure 4.6 and the threshold fluence for 1 pulse $F_{\mathrm{th}}(1)$ were estimated as intercept with y-axis. If the incubation coefficient $\xi = 1$, the incubation is absent. The values between 0 and 1 indicates, that material is weakened after the laser pulse [27]. The incubation in metals may be explained by a formation of voids and cracks in the resolidificated region, leading to significantly lower heat diffusion length compared to not treated by a laser (fresh) material [30].

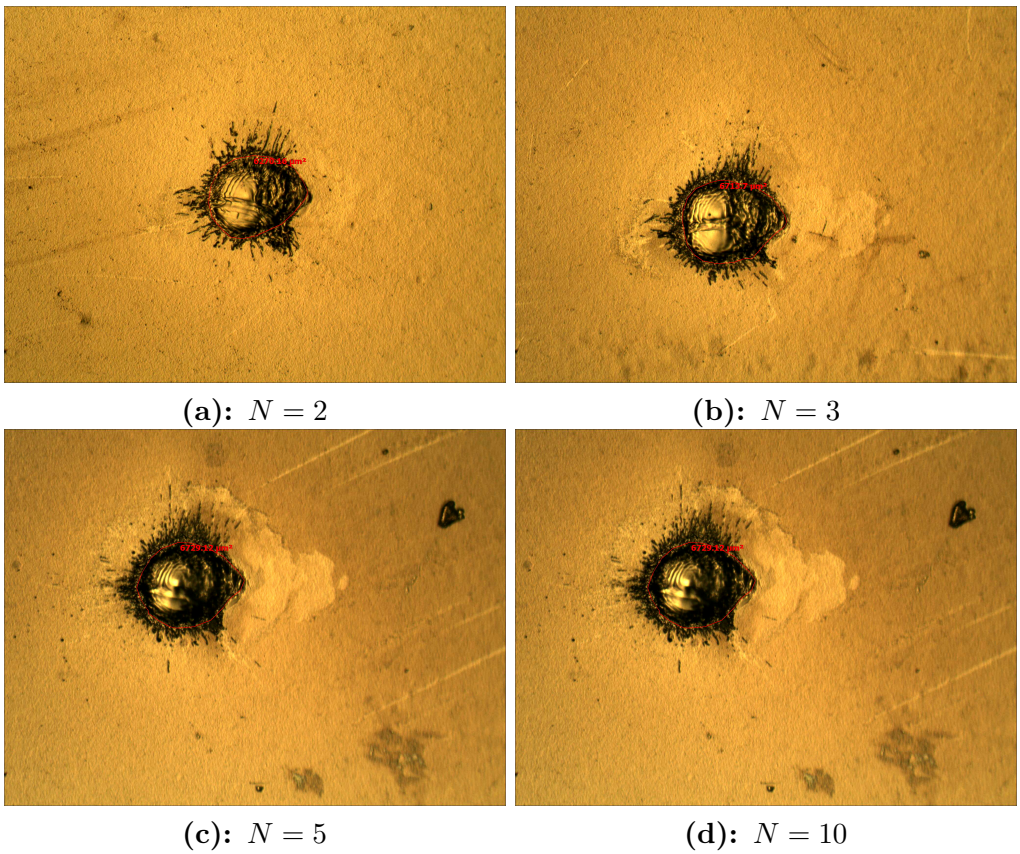

(a): $N = 2$ **(b):** $N = 3$

(c): $N = 5$ **(d):** $N = 10$

Figure 4.4: Ablation craters on the NiP-3 sample at532 nm and fluence 24.8 ± 2.5 J/cm^2 after different numbers of pulses. The square of the craters does not change with the increasing number of pulses. This demonstrates, that the incubation is absent.

The values of threshold fluence and incubation coefficient are presented in the Table 4.2. One can see, that Ni and Ni-P coatings represent low to negligible incubation at both 532 and 1064 nm. The value of the incubation coefficient at 532 nm is in good agreement with the literature values [29]. This observation shows, that the formation of voids and cracks leading to the change of the thermal properties play moderate role. The threshold fluence of Ni coatings is twice so high at 532 compared to 1064 nm. This phenomenon is still unclear and has to be the subject of the further research.

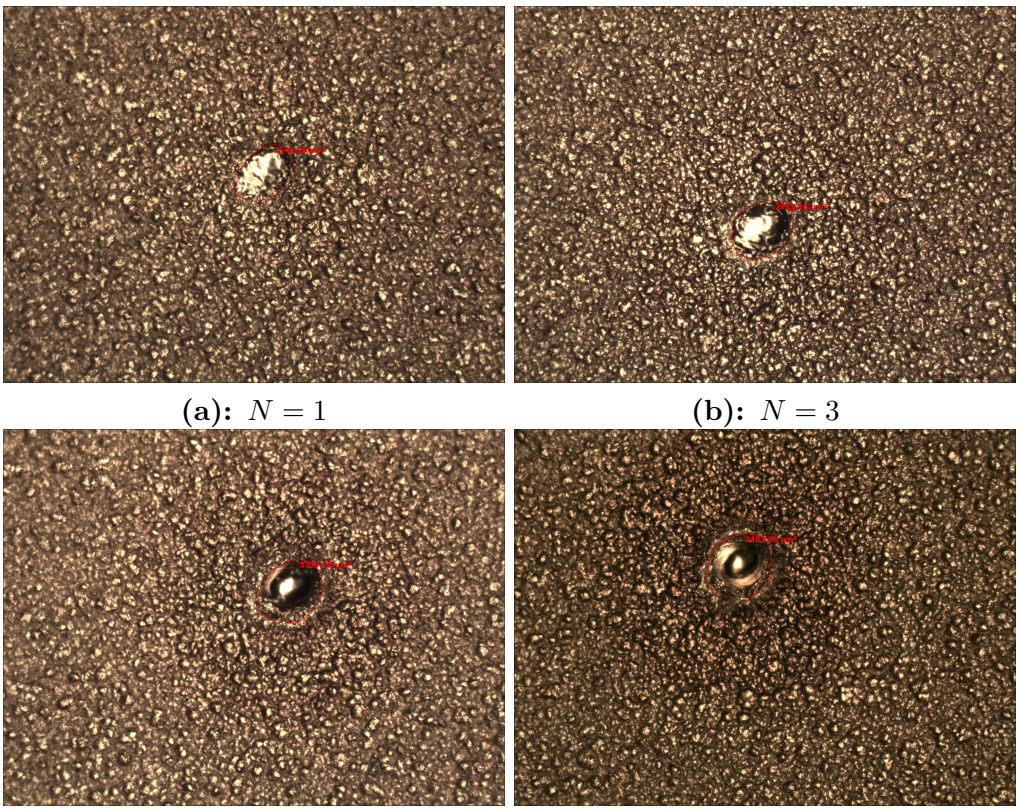

(a): $N = 1$ **(b):** $N = 3$

(c): $N = 5$ **(d):** $N = 10$

Figure 4.5: Ablation craters on the Cu-3 sample at 1064 nm and fluence 17.0 ± 1.7 J/cm^2 after different numbers of pulses, representing incubation behaviour. The square of the craters increases with the increasing number of pulses. This demonstrates the presence of the incubation.

Due to the high ablations rates of Cu, the incubation coefficient at 532 nm was not measured. In the infrared regime, Cu exhibits higher incubation compared to Ni and Ni-P. This suggests, that multiply defects accumulation take place, weakening the material and decreasing the threshold fluence. The threshold fluence of Cu is significantly higher compared to Ni, what correlates with the material properties. The theoretical threshold fluence was calculated using a simple model, described by the equation Equation 2.7 and compared with the experimental values Table 4.3. One can observe, that the experimen-

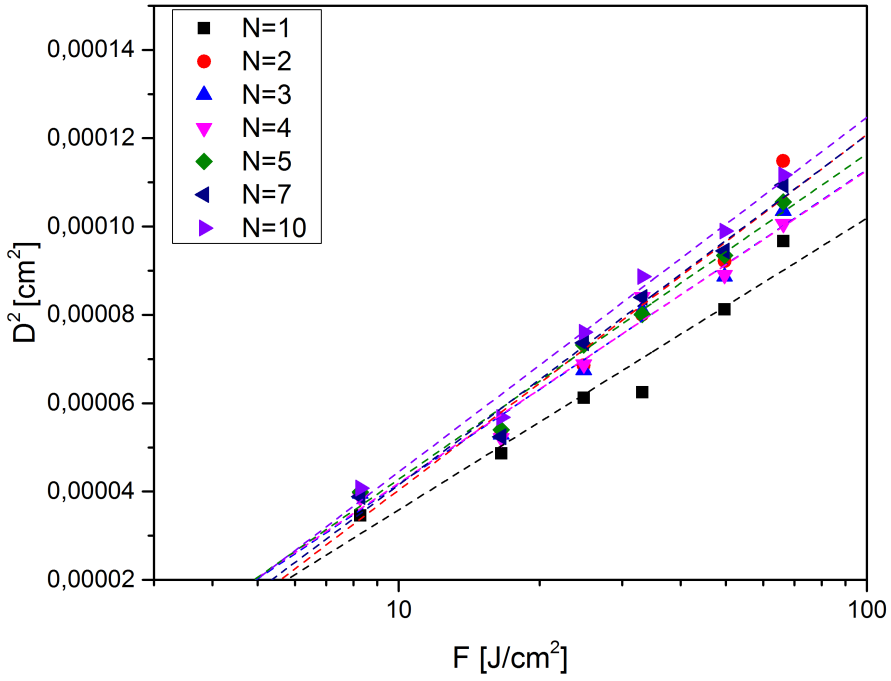

Figure 4.6: Threshold fluence and incubation coefficient determination on the NiP-3 sample at 532 nm.

tal value is in a good agreement with the theoretical for 532 nm. In contrary, the ablation at 1064 nm exceeds the theoretical values twice.

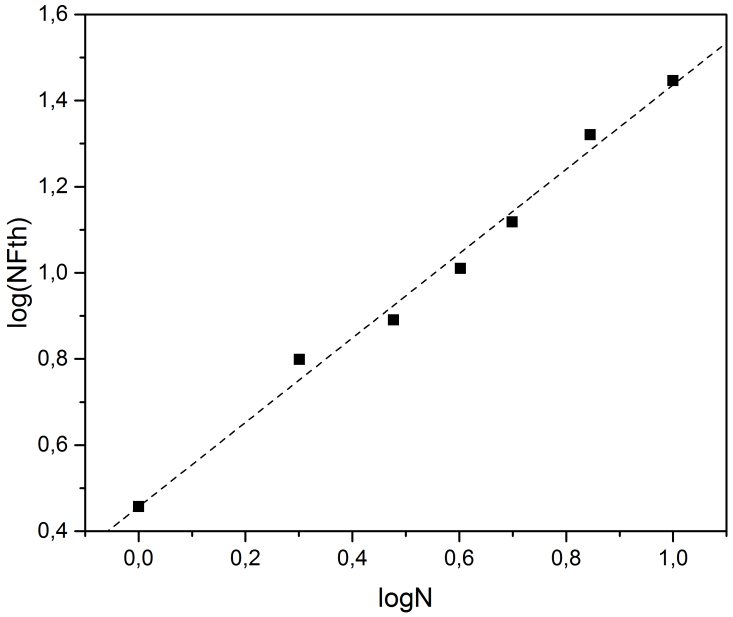

Figure 4.7: Determination of the incubation coefficient on the NiP-3 sample at 532 nm.

Table 4.2: Threshold fluence and incubation coefficient values for 532 and 1064 nm wavelength, calculated using D^2 method.

Sample ID	d [µm]	$F_{\text{th@532nm}}(1)$ [J/cm^2]	$\xi_{\text{@532nm}}$	$F_{\text{th@1064nm}}(1)$ [J/cm^2]	$\xi_{\text{@1064nm}}$
Ni-1	8.0	-	-	1.5±0.2	0.94±0.02
Ni-2	30.9	3.8±0.3	0.90±0.07	1.6±0.5	0.97±0.16
Ni-3	40	3.3±0.5	0.84±0.12	2.1±0.3	0.93±0.10
NiP-1	4.5	2.8±0.1	0.99±0.03	1.7±0.3	0.81±0.04
NiP-2	11.7	3.1±0.3	1.01±0.08	1.5±0.4	0.88±0.07
NiP-3	23.0	3.0±0.2	0.94±0.03	1.3±0.5	0.85±0.05
Cu-1	13.9	-	-	-	-
Cu-2	18.7	-	-	3.5±0.5	0.76±0.13
Cu-3	20.7	-	-	2.9±0.1	0.81±0.12

Table 4.3: Averaged experimental threshold for 532 and 1064 nm wavelength compared with the theoretical values [32].

Material	$F_{\text{th@532nm}}(1)$ [J/cm^2]	$F_{\text{th@1064nm}}(1)$ [J/cm^2]	Theoretical $F_{\text{th@532nm}}(1)$	Theoretical $F_{\text{th@1064nm}}(1)$
Ni	3.6±0.4	1.7±0.4	2.7	3.2
Cu	-	3.2±0.4	-	5.4

4.3 LIBS-stratigraphy

After the threshold fluence was calculated, the LIBS-stratigraphy measurements was performed at 532 and 1064 nm wavelength. [1] Each measurement were made at 25 spots, each 100 pulses deep to improve the signal-to-noise ratio. All depth profiling measurements were performed varying pulse energy/fluence as presented in the Table 4.4. The fluence difference at different wavelength explains by the value of Gaussian beam radius (62 µm and 75 µm at 532 and 1064 nm respectively). This results higher fluence at 532 nm at same pulse energy.

A linear correlation method (Pearson) described in subsection 3.4.1, based on an using total spectral information to compare a similarity between spectra measured and standard spectra, was applied in this work. This method has the advantage of eliminating experimental noise like laser fluence fluctuations, pulse-to-pulse fluctuations in plasma density and temperature and signals resulting from point impurities in a material in the resulting depth profiles [6, 18, 19].

Therefore, the spectrum of pure Ni, since Ni is the major element in all Ni-containing coatings, and pure Cu were chosen as standards for coating material. Pure Fe spectrum was used to represent steel substrate. The standard spectra with peaks identified are presented on the Figure 4.8, Figure 4.9, Figure 4.10. Fe and Ni are transition metals having open *d*-shell, what makes a lot of transition possible. For this reason spectra of this elements are characterized by high number of transition, what explains the high number of the spectral lines obtained. The resulted stratigrams were fitted by the empirical exponential rise and decay function, described in subsection 3.4.2.

[1] Parts of the results and findings of this section have been accepted to publish in *Applies Physics A* [55] and presented at the Spring Meeting of the European Material Research Society (EMRS), Strasbourg, France, 22-26.05.2017.

Table 4.4: Laser pulse energy and corresponding fluence applied in the LIBS experiments.

Energy [μJ]	0.13	0.26±0.03	0.39±0.04	0.52±0.05	0.78±0.08	1.04±0.10
Fluence 532 nm [J/cm^2]	2.2±0.2	4.3±0.4	6.5±0.7	8.6±0.9	12.9±1.3	17.2±1.7
Fluence 1064 nm [J/cm^2]	1.5±0.2	2.9±0.3	4.4±0.4	5.8±0.6	8.8±0.9	11.7±1.2

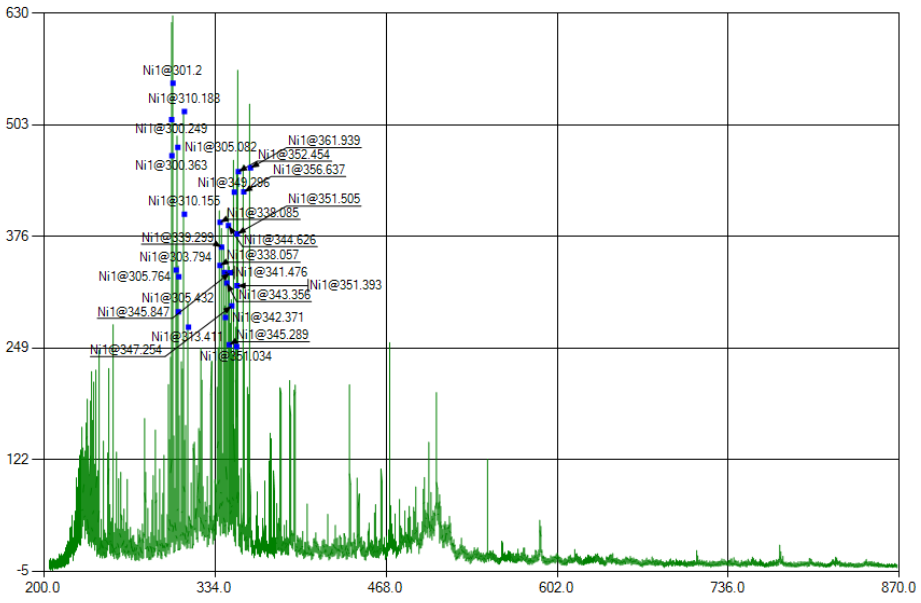

Figure 4.8: Spectrum obtained by averaging the spectra of 100 laser pulses on pure Ni with the peaks identified [56].

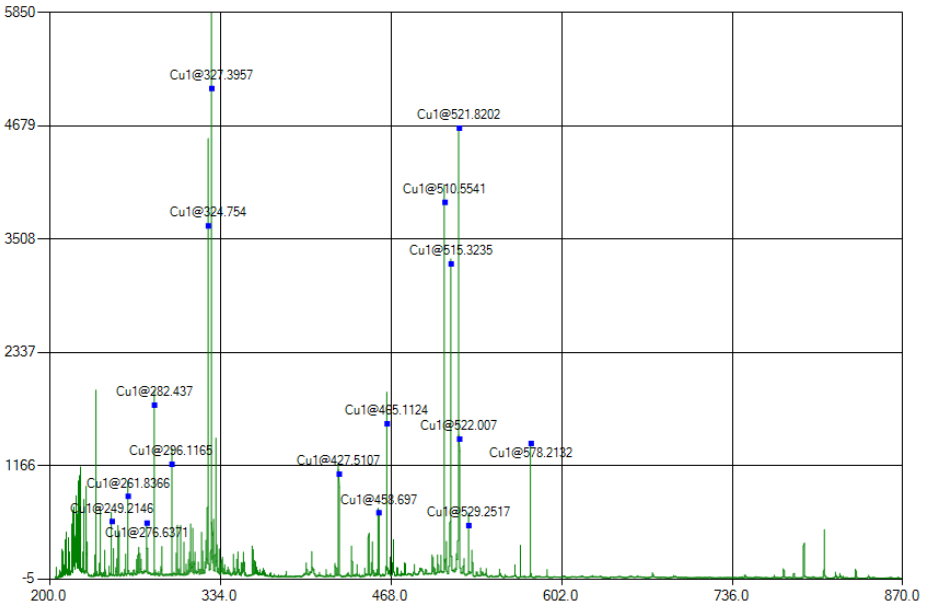

Figure 4.9: Spectrum obtained by averaging the spectra of 100 laser pulses on pure Cu with the peaks identified [56].

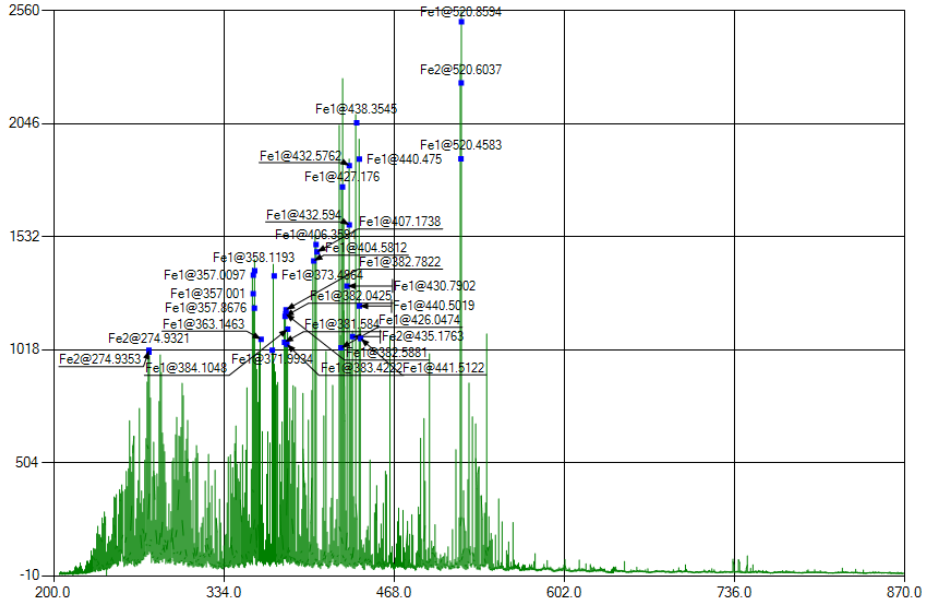

Figure 4.10: Spectrum obtained by averaging the spectra of 100 laser pulses on pure Fe with the peaks identified [56].

4.3.1 Electroplated Ni and electroless Ni-P coatings

Electroplated Ni

Figure 4.11 shows spectra (averaged over 25 recordings) of a Ni on steel sample after 2 (c), 30 (d) and 70 (e) and standard spectra of Ni (a) and Fe (b) for comparison. After the very first few pulses(c), only the coating element is ablated and the spectra recorded coincide with the spectra of pure Ni. After the breach of the coating, the substrate is ablated and the emission lines of Fe emerge (d). Due to the Gaussian laser beam profile, not only the valley of the crater is affected by the plasma pulse, also the slopes are irradiated. Even though the laser fluence here drops below the ablation threshold of fresh material, incubation effects lead to an additional broadening of the craters, shaping them Gaussian-like [18, 19, 27]. This explains the presence of the emission lines of the coating material in the spectra recorded subsequent to the breach of the coating layer. As a consequence, the emergence of the underlying material's signal (Fe signal representing steel) was used as the indicator of the layer breach (derived in subsection 3.4.2). The schematically images of formated craters are presented on the left part of Figure 4.11. The crater diameters are increasing due the incubation effect.

The experiments were carried out varying the laser fluence according to Table 4.4. Figure 4.12 shows the influence of the fluence on the signal-to-noise ratio, represented by a higher Pearson correlation coefficient. The number of pulses needed to achieve the layer breach are generally lower at the higher fluence due to the higher average ablation rate h and improvement of the signal-to-noise ratio. The zero correlation at the laser pulse energy 0.5 mJ/pulse can be explained by too low energy to formate the plasma, though the material was ablated.

Similar behaviour is obtained at 1064 nm. The correlation coefficient is rising with the increase of the laser pulse fluence. The calculated correlation

coefficient r is though higher and number of pulses to breach through the coating is higher compared to the measurements at 532 nm.

The averaged ablation rates h were calculated by dividing the layer thickness determined by EDX-spectroscopy to the number of pulses needed to breach through the coating $N^i_{(j-1,j)}$, which was determined by fitting the data using exponential rise and decay function described in subsection 3.4.2. For the determination of the layer thickness the correlation trace of Fe has been used, because of its sharp rising edge at the layer boundary, which has a higher reproducibility in experiments with the same experimental parameters compared to the traces of coating [19].

The Figure 4.14 represents depth correlation stratigrams of Ni-3 at fluence 12.9 ± 1.3 J/cm^2 for 532 nm wavelength and at a maximum fluence of 11.7 ± 1.2 J/cm^2 for 1064 nm, compared to the EDX line scans, used for layer thickness determination. One can observe that for Ni, more laser are needed to ablate a layer of the same thickness with an infrared (1064 nm) laser pulse, than with a visible (532 nm) one at a defined fluence. Thus shows the clear wavelength dependence of the ablation rates.

The calculated ablation rates were plotted against the fluence. When the laser beam has a Gaussian profile, the ablation rates are expected to follow a logarithmic relation [27, 28]:

$$h(F) = \frac{1}{\alpha_{\text{eff}}} \ln\left(\frac{F}{F_{\text{th}}}\right) \tag{4.1}$$

where α_{eff} is the effective absorption coefficient and can be determined as the slope of the semi-logarithmic plots of averaged ablation rates h vs maximal fluence F (Figure 4.15). Figure 4.16 represents the effective absorption coefficient α_{eff} for all Ni-samples at two wavelength. The ablation rates yielded higher values of absorption coefficient in the infrared regime, compared to the visible range. No thickness dependence can be obtained from the presented results.

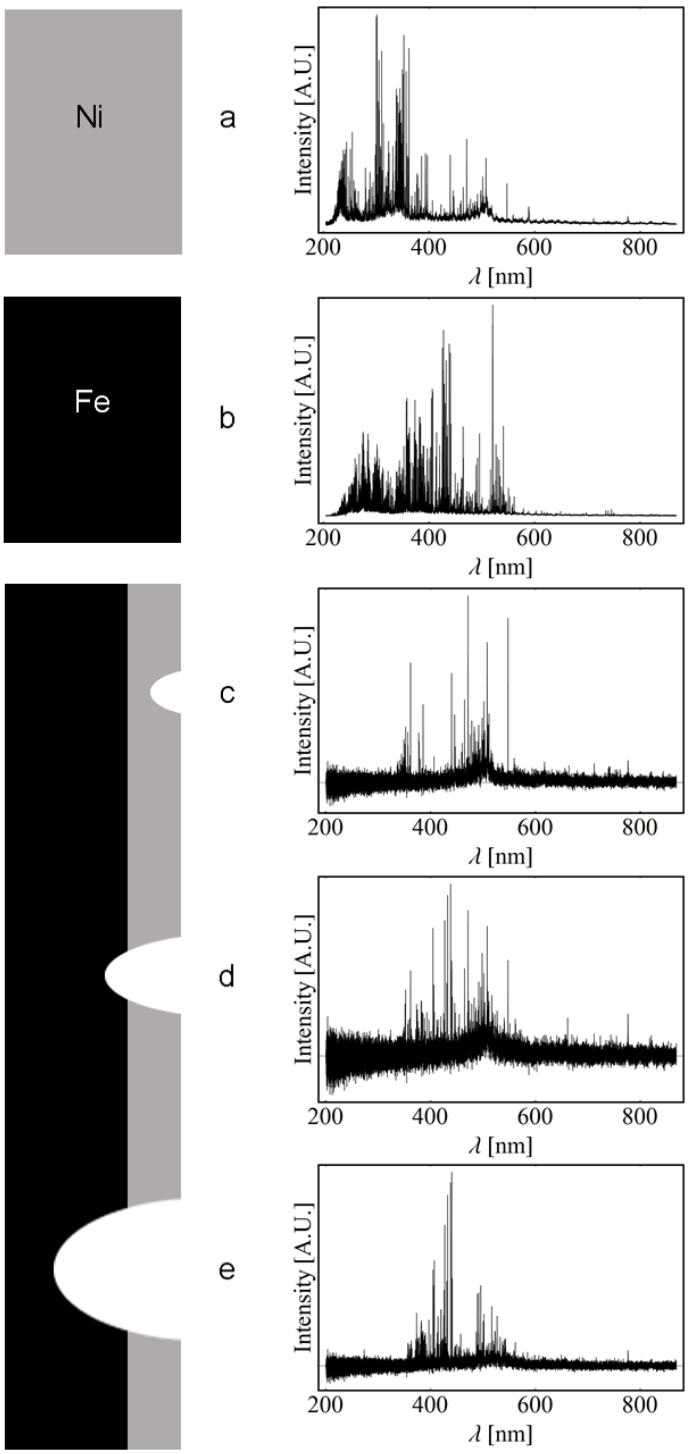

Figure 4.11: Standard spectra of Ni (a), Fe (b) used for Pearson correlation and averaged spectra recorded at 1064 nm on the Ni-3 sample after 2 (c), 30 (d) and 70 (e) pulses. The schematic image of the coated material with the Gaussian shape ablation craters is presented on the left side.

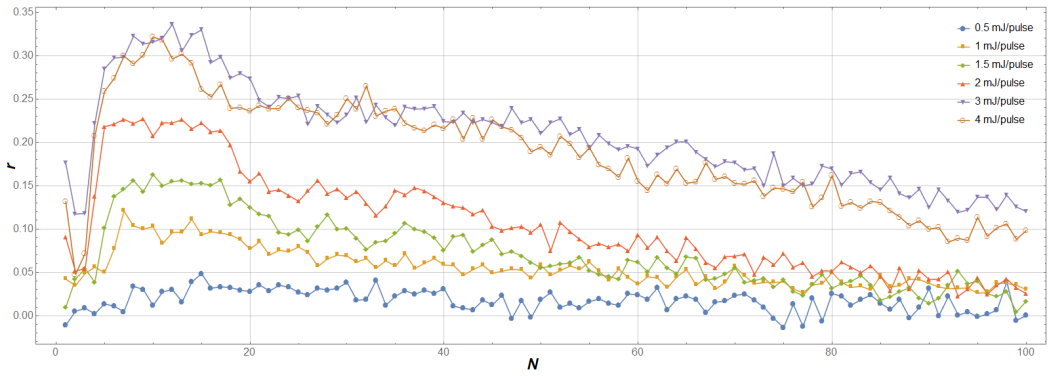

Figure 4.12: Stratigrams of the Ni-1 sample recorded at 532 nm, representing the influence of the laser pulse energy on the correlation coefficient (Fe trace) and the number of pulses needed to breach through the coating.

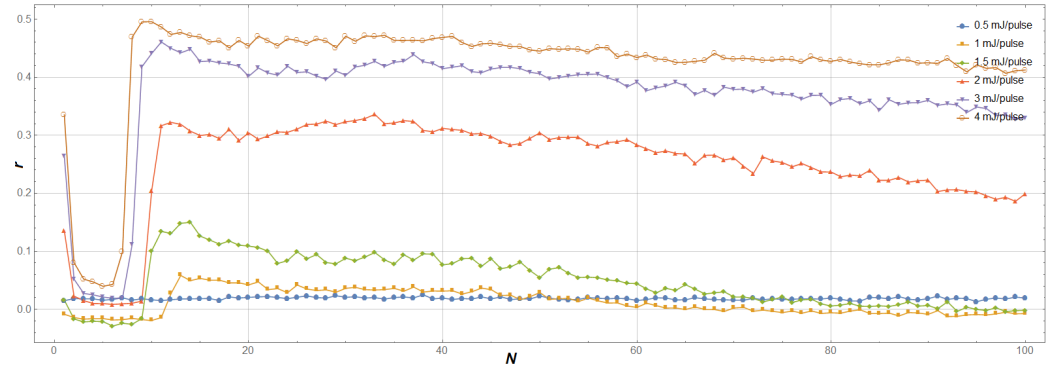

Figure 4.13: Stratigramms of Ni-1 sample obtained at 1064 nm, representing the influence of the laser pulse energy on the correlation coefficient (Fe trace) and the number of pulses needed to breach through the coating.

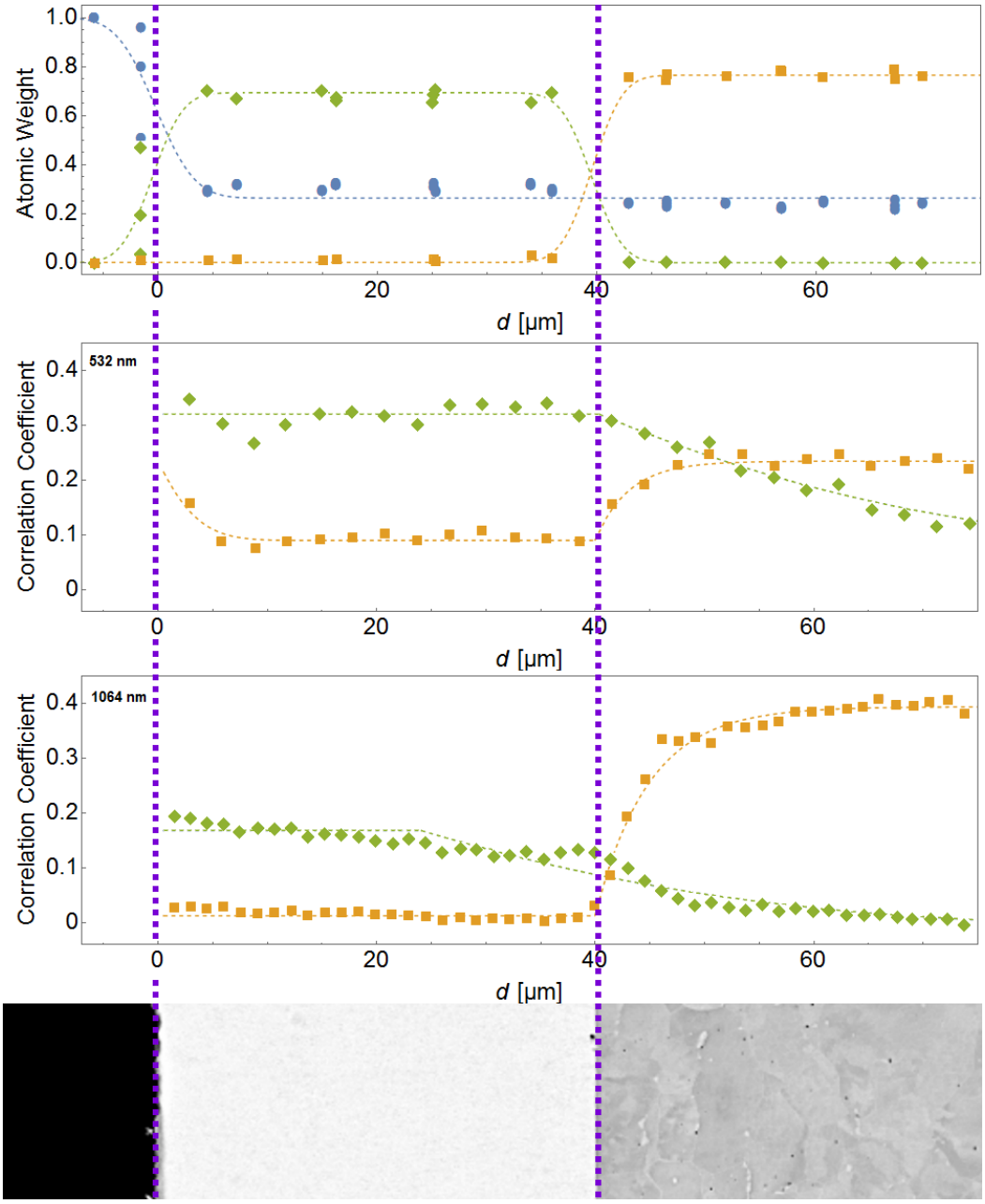

Figure 4.14: Comparison of the EDX-spectroscopy data of the Ni-3 sample (top) to the LIBS-correlation stratigrams recorded with 532 nm at a maximum fluence of 12.9 ± 1.3 J/cm^2 and 1064 nm at a maximum fluence of 11.7 ± 1.2 J/cm^2. •: Ni, ■:Fe. The vertical (violet) dashed lines indicate the beginning of the exponential rise.

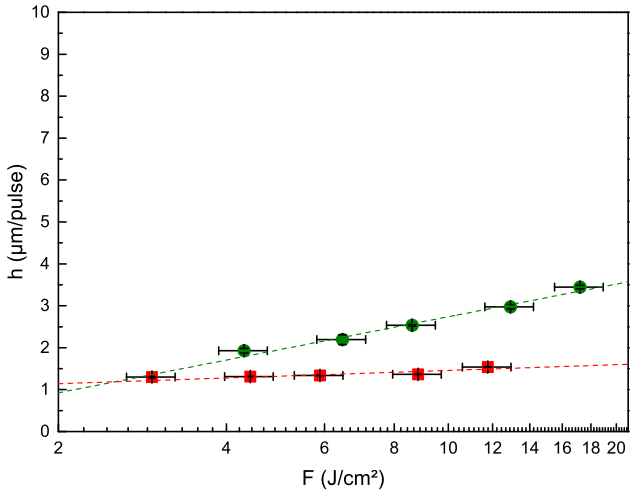

Figure 4.15: Fluence dependency of ablation rates of the Ni-3 at •: 532 nm, ■: 1064 nm. The dashed lines fit linearly to the measured data. A slope of this graphs gives the value of the effective absorption coefficient α_{eff}.

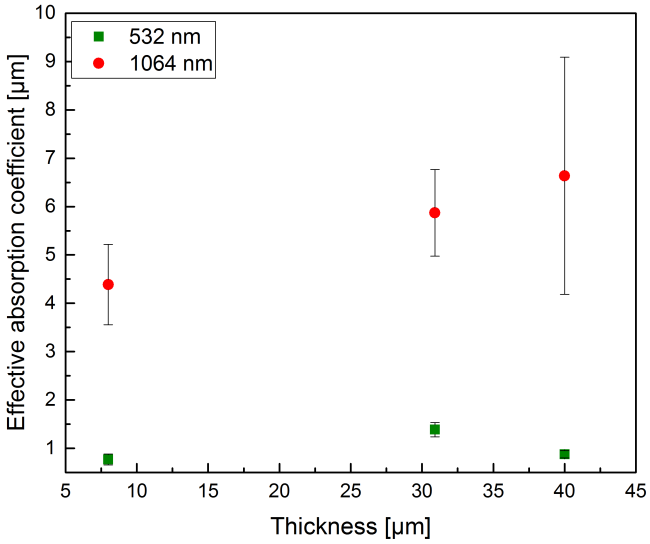

Figure 4.16: Effective absorption coefficient of Ni, calculated for the different thickness of coating and two wavelength.

Ni-P alloy

The similar behaviour was also obtained for Ni-P samples. The Figure 4.17 and Figure 4.18 represents the exemplary stratigrams recorded on NiP-2 sample varying the laser pulse energy (fluence). One can see that at the lowest energies no signal is obtained, for the reason, that the laser pulse energy is too low to ignite a plasma. At the higher energy, the correlation coefficient increases, because the signal-to-noise ratio improves. At the higher fluence, lower number of pulses is needed to breach through the layers and the ablation rates increase. The higher correlation coefficient and better signal-to-noise ratio is obtained at 1064 nm compared to 532 nm.

The ablation rates were plotted versus the fluence and slope of the graph gives the value of the effective absorption coefficient (Figure 4.19). In analogy to the electroplated Ni coatings, the strong wavelength dependency was obtained.

In the same way as electroplated Ni, electroless Ni-P shows the lower ablation rates and the higher effective absorption coefficient α_{eff} at 1064 compared to 532 nm Figure 4.20, resulting in the better depth resolution of the LIBS-stratigraphy.

Additionally, the ablation rate of electroless Ni is lower compared to the electroplated Ni. The difference between α_{eff} of Ni and Ni-P can be attributed to differences in the plating process, what influence also the thermal properties of the coatings. The thermal conductivity of the Ni-P is one order of magnitude lower compared to electroplated Ni [57], what results in the differences in the thermal diffusion length and consequently in the ablation behaviour.

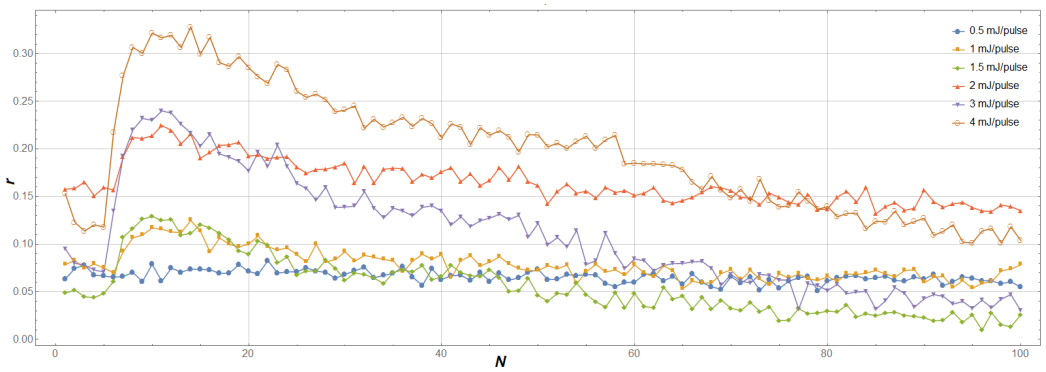

Figure 4.17: Stratigrams of the NiP-2 sample, recorded at 532 nm, representing the influence of the laser pulse energy on the correlation coefficient r value and the number of pulses needed to breach through the coating.

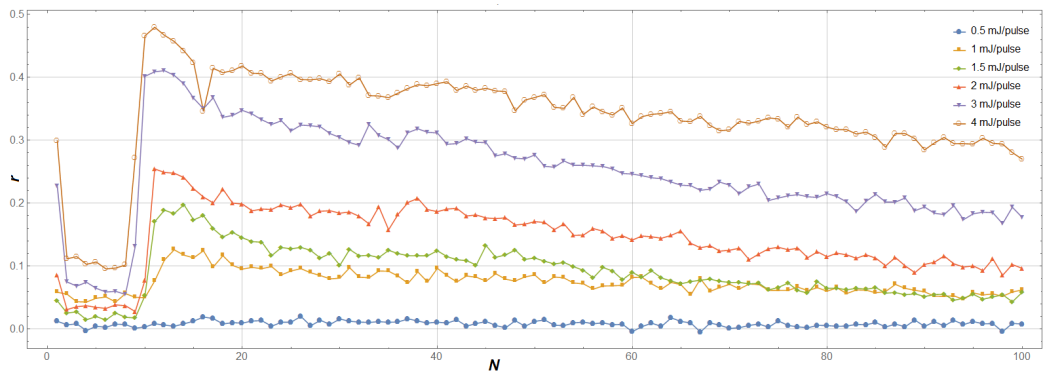

Figure 4.18: Stratigrams of the NiP-2 sample recorded at 1064 nm, representing the influence of the laser pulse energy on the correlation coefficient r value and the number of pulses needed to breach through the coating.

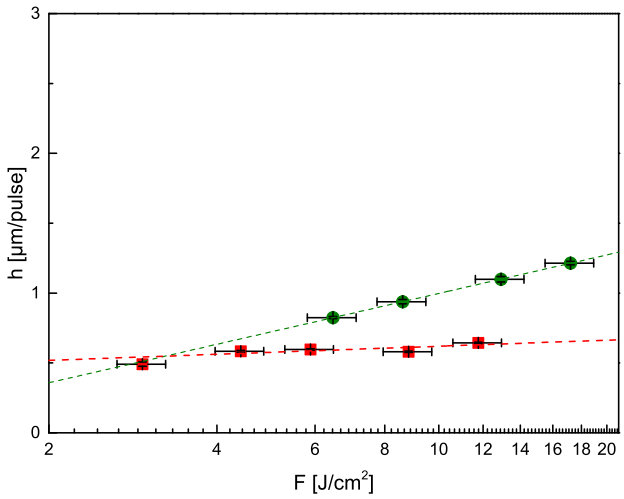

Figure 4.19: Fluence dependency of the ablation rates of NiP-3 at •: 532 nm, ■: 1064 nm. The dashed lines fit linearly to the measured data. A slope of this graphs gives the value of the effective absorption coefficient α_{eff}.

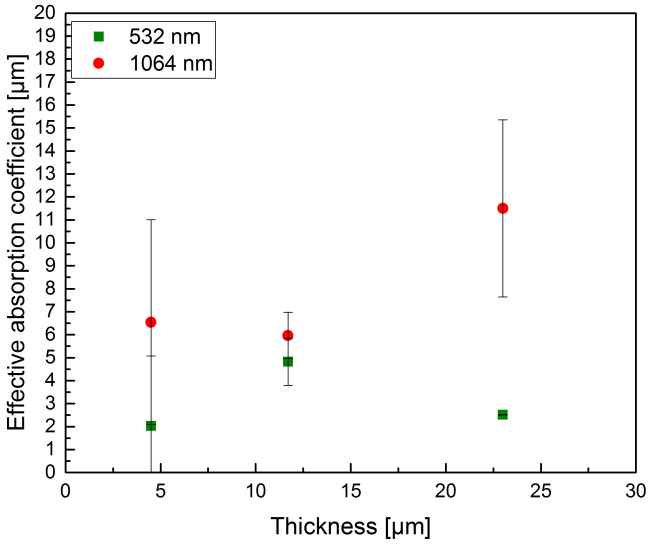

Figure 4.20: Effective absorption coefficient α_{eff} of Ni-P alloy at 532 nm (green) and 1064 nm (red).

4.3.2 Cu coatings

The same procedure was applied to the Cu/steel system. The Figure 4.21 represents the spectra after 2, 12 and 70 compared with standards of Cu and Fe. At the first pulses, the ablation of coating material is taking place and the spectrum obtained coincides with the pure Cu. After the breach of the layer, the emission lines of Fe rise and the Cu is present, due to incubation effect and Gaussian-like craters shape (described in subsubsection 4.3.1). After the additional pulses, the Cu signal drops significantly.

The exemplary stratigrams for the both wavelength are presented in Figure 4.22 and Figure 4.23. The lowest pulse energy gives zero correlation, what shows, that no plasma is ignited at this energy. As expected, the correlation coefficient rises with increase of the pulse fluence and less pulses are needed to ablate the coating. With higher number of pulses, the signal decays. This is caused by the elemental self-absorption, which is the more present the more plasma is confined in an ablation crater. The confinement results in more optically dense plasma. Additionally, the higher signal-to-noise ratio is obtained in infrared regime.

Similarly to Ni, more pulses are needed to drill through the coating, using 1064 nm irradiation. As an example, at the 532 nm laser pulse with maximal fluence of 12.9 $\pm$ 1.3 J/cm^2, only around 3 pulses are needed to breach the coating of 17.7 µm. By the infrared pulse (11.7 $\pm$ 1.2 J/cm^2) the coating is ablated after 11 pulses.

Figure 4.25 shows the calculated ablation rates as function of fluence. As expected the ablation rates h rise logarithmic with fluence. The slope of the linear fit yields the value of α_{eff} (Figure 4.26). The resulted values do not show any thickness dependence in the investigated range.

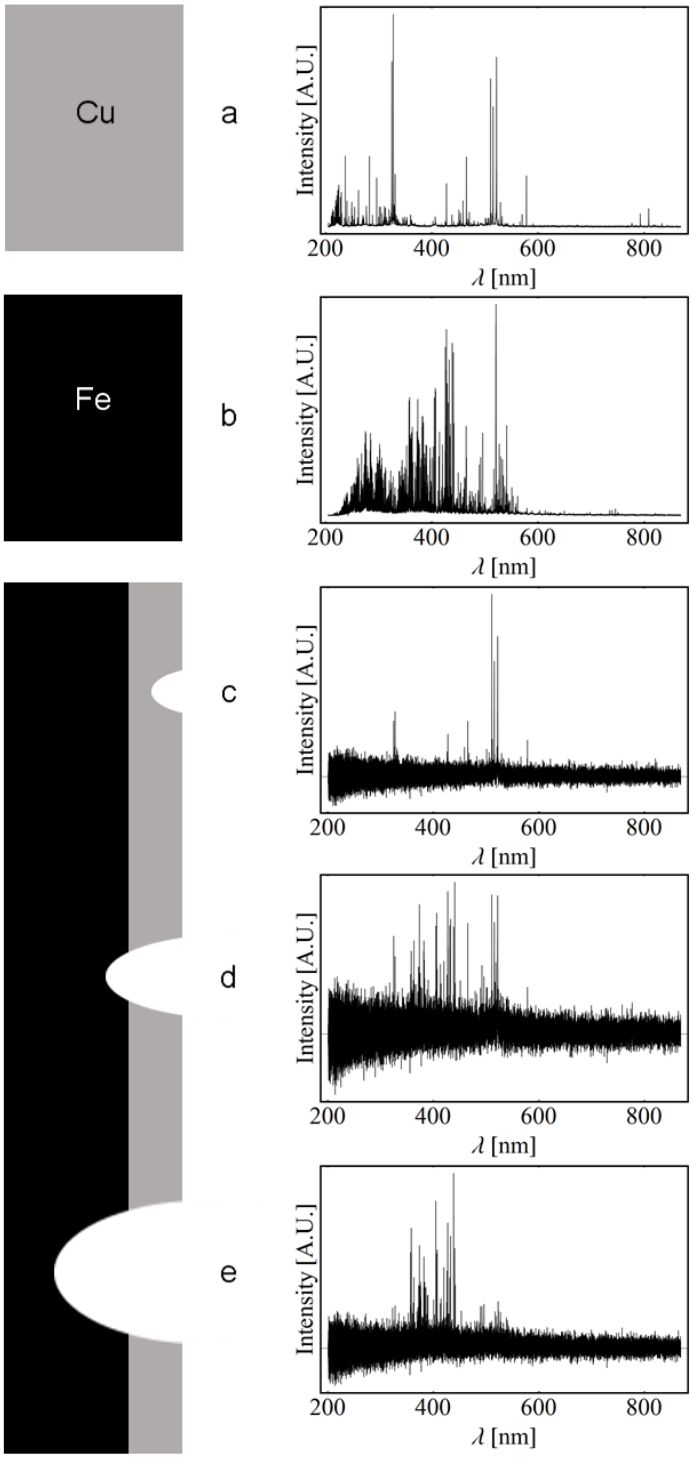

Figure 4.21: Standard spectra of Cu (a), Fe (b) used for Pearson correlation and the averaged spectra recorded at 1064 nm at maximal fluence 11.7 ± 1.2 J/cm^2 on the Cu-2 sample after 2 (c), 12 (d) and 70 (e). The schematic image of coated material with Gaussian-like shape ablation craters is presented on the left side.

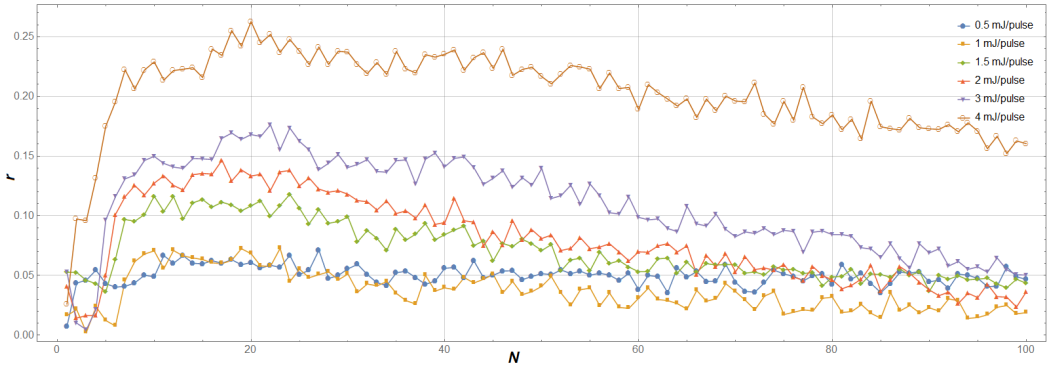

Figure 4.22: Stratigrams of the Cu-2 sample recorded at 532 nm representing the influence of the laser pulse energy on the correlation coefficient and the number of pulses needed to breach through the coating.

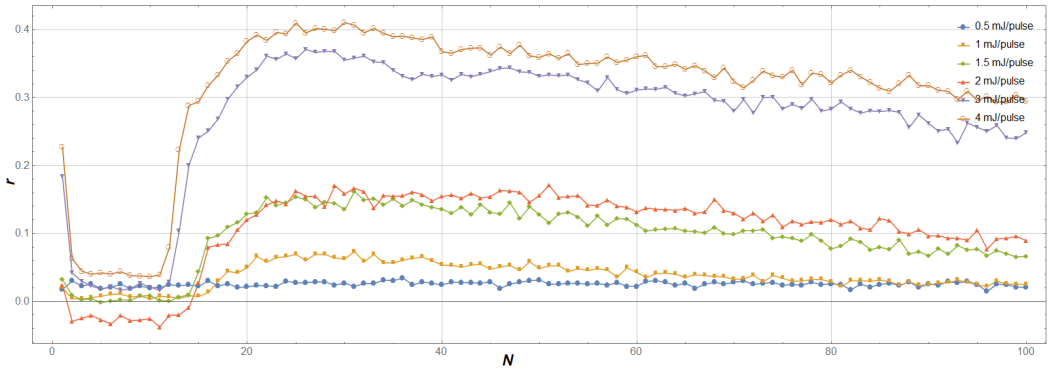

Figure 4.23: Stratigrams of the Cu-2 sample recorded at 1064 nm representing the influence of the laser pulse energy on the correlation coefficient and the number of pulses needed to breach through the coating.

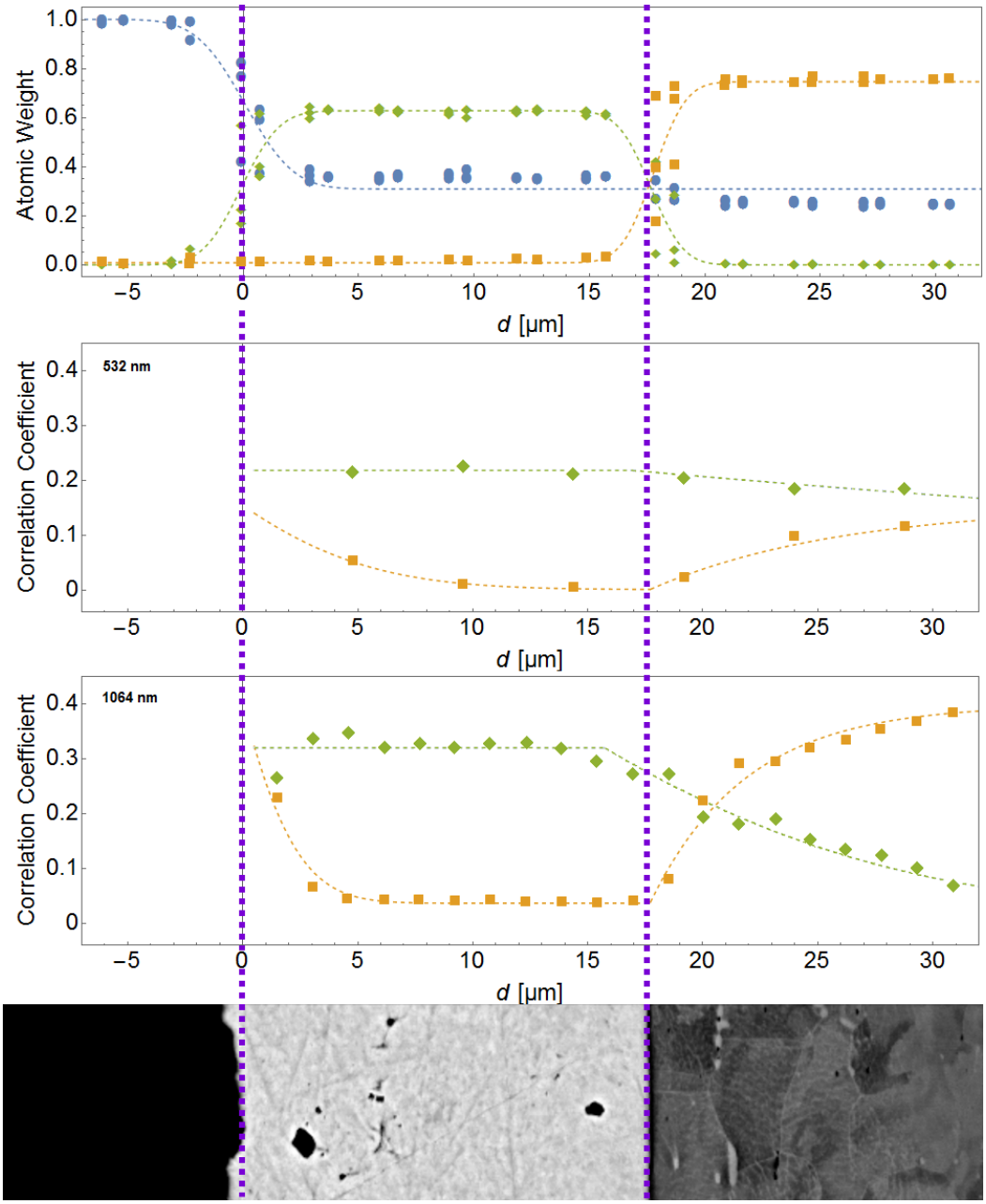

Figure 4.24: Comparison of the EDX-spectroscopy data of the Cu-2 plated sample (top) to the LIBS-correlation stratigrams recorded with 532 nm at a maximum fluence of 12.9 ± 1.3 J/cm^2 and 1064 nm at a maximum fluence of 11.7 ± 1.2 J/cm^2. •: Cu, ■:Fe. The vertical (violet) dashed lines indicate the beginning of the exponential rise. A BSE image is presented at the bottom.

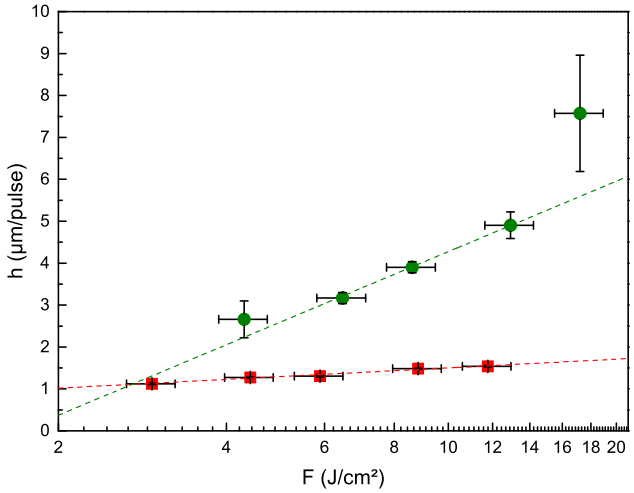

Figure 4.25: Fluence dependency of the ablation rates of Cu at •: 532 nm, ■: 1064 nm. The dashed lines fit linearly to the measured data. A slope of this graphs gives the effective absorption coefficient α_{eff}.

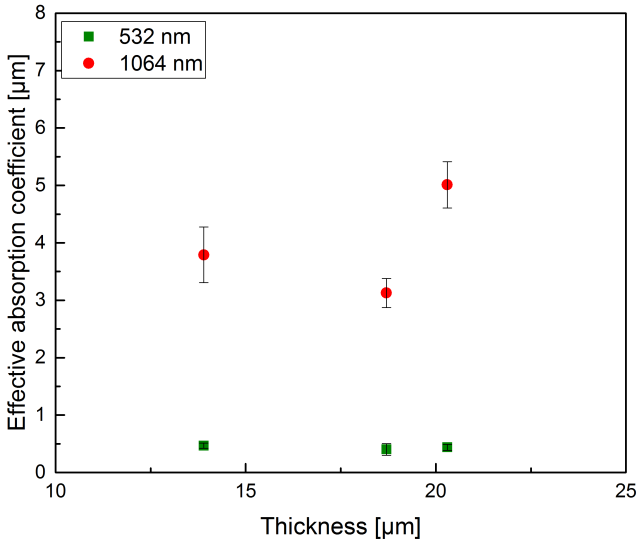

Figure 4.26: The effective absorption coefficient of Cu at 532 and 1064 nm.

4.3.3 Comparison of effective absorption coefficient with modelled values

The averaged effective absorption coefficients evaluated in subsubsection 4.3.1, subsubsection 4.3.1 and subsection 4.3.2 are depicted in Figure 4.27 and collected in Table 4.5. NiP shows the highest values in respect to Ni and Cu. Moreover, there is a remarkable dependence on the wavelength.

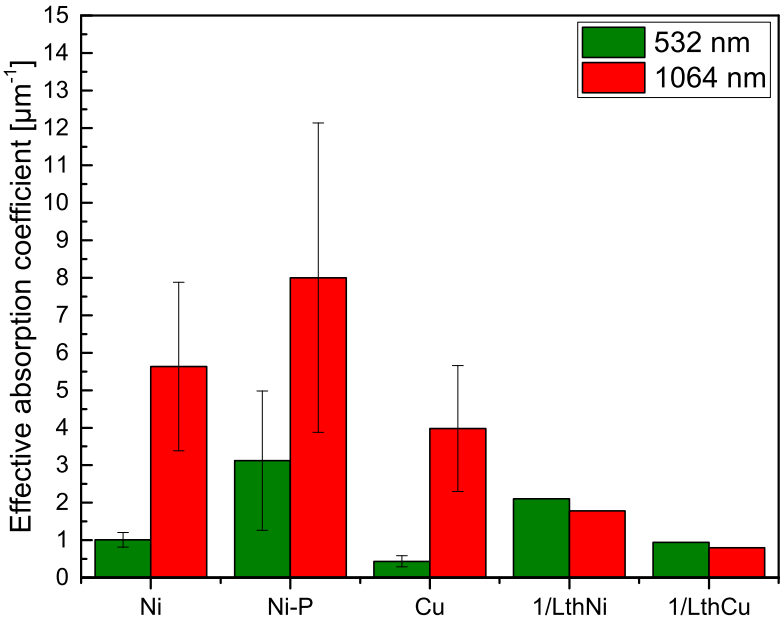

Figure 4.27: Effective absorption coefficient α_{eff} compared with thermal diffusion length for Ni and Cu.

For all materials, the values of α_{eff} at 1064 nm exceed the values at 532 nm. That means that the ablation rate is strongly wavelength-dependent.

The optical properties cannot be made responsible for this remarkable effect. The optical absorption coefficient α_{opt} of the coatings is an order

Table 4.5: Comparison of measured values of effective absorption coefficient α_{eff} and effective penetration depth L_{eff} with optical absorption coefficient α_{opt} [58,59], optical penetration depth L_{opt} and thermal diffusion length L_{th} [60]

	$\alpha_{\text{opt.}}$ [μm^{-1}]	α_{eff} [μm^{-1}]	$L_{\text{opt.}}$ [μm]	$L_{\text{eff.}}$ [μm]	L_{th} [μm]
Ni@532 nm	83	1.01±0.19	0.012	0.99±0.19	0.48
Ni@1064 nm	69	5.63±2.25	0.014	0.18±0.07	0.56
Cu@532 nm	61	0.43±0.14	0.016	2.32±0.76	1.05
Cu@1064 nm	83	3.97±1.68	0.012	0.25±0.11	1.25

of magnitude higher than α_{eff} obtained in this work. This translates to an optical penetration depth L_{opt} in the nanometre range, which is negligible in comparison to the thermal diffusion length L_{th} and also the effective diffusion length L_{eff}, which are in the micrometer regime (compare Table 4.5).

The thermal ablation model can explain the values of α_{eff} and L_{eff}, respectively [19, 23]:

$$\frac{1}{\alpha_{\text{eff}}} \propto L_{\text{th}} = \sqrt{2\kappa\tau} \tag{4.2}$$

where κ is thermal diffusivity and τ is pulse duration. Theoretical values of L_{th} [60] are presented in Figure 4.27 and Table 4.5 for comparison. The respective values of Ni-P was not found in the literature. L_{eff} and L_{th} exhibit the same order of magnitude.

An explanation of wavelength-dependent ablation behaviour could be plasma shielding, the absorption or scattering of laser pulse energy by a plasma. There are two mechanisms: inverse bremsstrahlung and photoionisation [61, 62]. The absorption coefficient of inverse bremsstrahlung is described by

$$\alpha_{\text{IB}} = 1.37 * 10^{-35} \lambda^3 n_e^2 T_e^{-1/2} \tag{4.3}$$

where λ is the laser wavelength, n_e the number electron density and T_e the electronic temperature. The photoionisation absorption coefficient is approximated by

$$\alpha_{PI} = 2.9 * 10^{-17} \frac{\epsilon_n^{5/2}}{(h\nu)^3} N_n \tag{4.4}$$

where $h\nu$ is the photon energy, ϵ_n the ionisation energy and N_n the number density of excited states.

The Equation 4.3 shows, that the influence of inverse bremsstrahlung absorption is much more effective in the IR regime. That leads to a reduction of ablation rates because less fluence arrives on the target due to shielding.

The photoionisation can be significant at shorter wavelengths, due to the higher photon energy, but the decreasing of ablation rates at 532 nm take place at higher fluences [61].

The plasma shielding can not only can explain lower ablation rates, but also an increase of the plasma emission, i.e. an increase of correlation coefficients in the IR regime. The plasma temperature increases due to absorption of the laser pulse, leading to additional heating of the plasma and increase of the signal-to-noise ratio, i.e. sensitivity. The same principle is used in double-pulse LIBS [47, 63–65]. The application of IR irradiation for LIBS depth-profiling showed a high influence of the plasma shielding, leading to higher depth resolution combined with higher sensitivity.

Chapter 5

Conclusions

The applicability and feasibility of LIBS for depth profiling has been shown with model coating systems such as electroplated nickel and copper, and electroless nickel-phosphorous.

LIBS exhibits the advantage that it allows an elemental analysis, that it is almost non-destructive, and it can be applied on any shape of a substrate in contrast to common depth profiling methods which are only applicable on flat samples.

The measured spectra were analysed with the Pearson linear correlation in order to avoid the drawbacks of the single emission line evaluation method.

The ablation rate can be correlated to the thermal diffusion length of the respective metallic materials. The optical properties expressed by the respective optical absorption coefficients are insignificant.

The ablation rate depends strongly on the wavelength. This finding cannot be explained by the optical absorption or the thermal diffusion length. Plasma shielding due to inverse bremsstrahlung increasing with the wavelength can be made responsible for the reduced ablation rate in the near infrared range.

These results show that the beam-plasma interaction not only plays an important role in the quantification of the ablation rate, the depth resolution

and the analysis depth, but also in the plasma heating which affects the plasma emission efficiency.

Thus, plasma shielding can support a higher depth resolution paralleled by a sensitivity increase due to plasma heating. Actually, a trade-in between depth resolution and sensitivity between visible and infrared has to be considered in practical cases. The present study suggests that the application of infrared radiation results in both a better emission efficiency and depth resolution.

Bibliography

[1] L. Radziemski, D. Cremers, A brief history of laser-induced breakdown spectroscopy: From the concept of atoms to libs 2012, Spectrochimica Acta Part B: Atomic Spectroscopy 87 (Supplement C) (2013) 3 – 10.

[2] D. A. Cremers, L. J. Radziemski, Handbook of Laser-Induced Breakdown Spectroscopy, John Wiley and Sons, Ltd, 2006.

[3] D. A. Cremers, R. C. Chinni, Laser-Induced Breakdown Spectroscopy-Capabilities and Limitations, Applied Spectroscopy Reviews 44 (6) (2009) 457–506.

[4] R. Noll, Laser-Induced Breakdown Spectroscopy Fundamentals and Applications, Springer-Verlag Berlin Heidelberg, 2012.

[5] D. A. Cremers, L. J. Radziemski, LASER-INDUCED BREAKDOWN SPECTROSCOPY (LIBS) Fundamentals and Applications, Cambridge University Press, New York, 2006, Ch. History and fundamentals of LIBS, pp. 1–39.

[6] M. P. Mateo, G. Nicolas, V. Piñon, A. Yañez, Improvements in depth-profiling of thick samples by laser-induced breakdown spectroscopy using linear correlation, Surface and Interface Analysis 38 (5) (2006) 941–948.

[7] V. Lednev, P. Sdvizhenskii, M. Filippov, M. Grishin, V. Filichkina, A. Stavertiy, R. Tretyakov, A. Bunkin, S. Pershin, Elemental profiling

of laser cladded multilayer coatings by laser induced breakdown spectroscopy and energy dispersive x-ray spectroscopy, Applied Surface Science 416 (2017) 302 – 307.

[8] S. Guirado, F. Fortes, V. Lazic, J. Laserna, Chemical analysis of archeological materials in submarine environments using laser-induced breakdown spectroscopy. on-site trials in the mediterranean sea, Spectrochimica Acta Part B: Atomic Spectroscopy 74 (Supplement C) (2012) 137 – 143.

[9] R. Noll, C. Fricke-Begemann, M. Brunk, S. Connemann, C. Meinhardt, M. Scharun, V. Sturm, J. Makowe, C. Gehlen, Laser-induced breakdown spectroscopy expands into industrial applications, Spectrochimica Acta Part B: Atomic Spectroscopy 93 (Supplement C) (2014) 41 – 51.

[10] D. Girón, T. Delgado, J. Ruiz, L. Cabalín, J. Laserna, In-situ monitoring and characterization of airborne solid particles in the hostile environment of a steel industry using stand-off libs, Measurement 115 (Supplement C) (2018) 1 – 10.

[11] V. Lazic, A. Palucci, S. Jovicevic, M. Carpanese, Detection of explosives in traces by laser induced breakdown spectroscopy: Differences from organic interferents and conditions for a correct classification, Spectrochimica Acta Part B: Atomic Spectroscopy 66 (8) (2011) 644 – 655.

[12] J. S. Caygill, F. Davis, S. P. Higson, Current trends in explosive detection techniques, Talanta 88 (Supplement C) (2012) 14 – 29.

[13] G. S. Senesi, Laser-induced breakdown spectroscopy (libs) applied to terrestrial and extraterrestrial analogue geomaterials with emphasis to minerals and rocks, Earth-Science Reviews 139 (Supplement C) (2014) 231 – 267.

[14] M. P. Mateo, J. M. Vadillo, J. J. Laserna, Irradiance-dependent depth profiling of layered materials using laser-induced plasma spectrometry, Journal of Analytical Atomic Spectrometry 16 (11) (2001) 1317–1321.

[15] A. Jurado-López, M. D. Luque de Castro, Laser-induced breakdown spectrometry in the jewellery industry. part i. determination of the layer thickness and composition of gold-plated pieces, J. Anal. At. Spectrom. 17 (5) (2002) 544–547.

[16] A. Jurado-López, M. D. Luque de Castro, Laser-induced breakdown spectrometry in jewellery industry. part ii: Quantitative characterisation of goldfilled interface, Talanta 59 (2) (2003) 409–415.

[17] M. Abdelhamid, S. Grassini, E. Angelini, G. Ingo, M. Harith, Depth profiling of coated metallic artifacts adopting laser-induced breakdown spectrometry, Spectrochimica Acta Part B: Atomic Spectroscopy 65 (8) (2010) 695 – 701.

[18] T. O. Nagy, U. Pacher, H. Pöhl, W. Kautek, Atomic emission stratigraphy by laser-induced plasma spectroscopy: Quantitative depth profiling of metal thin film systems, Applied Surface Science 302 (2014) 189 – 193.

[19] T. Nagy, U. Pacher, A. Giesriegl, M. Weimerskirch, W. Kautek, Depth profiling of galvanoaluminium–nickel coatings on steel by uv- and vis-libs, Applied Surface Science 418, Part B (2017) 508 – 516.

[20] J. M. Vadillo, J. Laserna, Laser-induced plasma spectrometry: truly a surface analytical tool, Spectrochimica Acta Part B: Atomic Spectroscopy 59 (2) (2004) 147 – 161.

[21] J. W. Dini, D. D. Snyder, Modern electroplating ed. by M. Schlesinger, M. Paunovic, 5th Edition, John Wiley & Sons, Inc., Hoboken, New Jersey, 2010, Ch. Electrodeposition of Copper, pp. 33–78.

[22] G. A. Di Bari, Modern electroplating ed. by M. Schlesinger, M. Paunovic, 5th Edition, John Wiley & Sons, Inc., Hoboken, New Jersey, 2010, Ch. Electrodeposition of Nickel, pp. 79–114.

[23] E. Matthias, M. Reichling, J. Siegel, O. W. Kading, S. Petzoldt, H. Skurk, P. Bizenberger, E. Neske, The influence of thermal-diffusion on laser-ablation of metal-films, Applied Physics A: Materials Science and Processing 58 (2) (1994) 129–136.

[24] L. H. J. Lajunen, Spectrochemical Analysis by Atomic Absorption and Emission, The Royal Society of Chemistry, 1992.

[25] A. P. Thorne, Spectrophysics, 2nd Edition, Chapman and Hall Ltd, 1988.

[26] J. Aguilera, C. Aragón, F. P. nalba, Plasma shielding effect in laser ablation of metallic samples and its influence on libs analysis, Applied Surface Science 127–129 (1998) 309–314.

[27] J. Krüger, W. Kautek, Ultrashort pulse laser interaction with dielectrics and polymers, Advances in Polymer Science 168 (2004) 247–289.

[28] D. Bäuerle, Laser Processing and Chemistry, 4th Edition, Springer Berlin Heidelberg New York, 2011.

[29] N. Lasemi, U. Pacher, C. Rentenberger, O. Bomatí-Miguel, W. Kautek, Laser-assisted synthesis of colloidal ni/niox core/shell nanoparticles in water and alcoholic solvents, ChemPhysChem 18 (9) (2017) 1118–1124.

[30] N. Lasemi, U. Pacher, L. Zhigilei, O. Bomatí-Miguel, R. Lahoz, W. Kautek, Pulsed laser ablation and incubation of nickel, iron and tungsten in liquids and air, Applied Surface Science 433 (Supplement C) (2018) 772 – 779.

[31] B. Neuenschwander, B. Jaeggi, M. Schmid, G. Hennig, Surface structuring with ultra-short laser pulses: Basics, limitations and needs for high throughput, Physics Procedia 56 (Supplement C) (2014) 1047 – 1058.

[32] L. Cabalín, J. Laserna, Experimental determination of laser induced breakdown thresholds of metals under nanosecond q-switched laser operation, Spectrochimica Acta Part B: Atomic Spectroscopy 53 (5) (1998) 723 – 730.

[33] Y. Jee, M. F. Becker, R. M. Walser, Laser-induced damage on single-crystal metal-surfaces, Journal of the Optical Society of America B-Optical Physics 5 (3) (1988) 648–659.

[34] A. Naghilou, O. Armbruster, W. Kautek, Femto- and nanosecond pulse laser ablation dependence on irradiation area: The role of defects in metals and semiconductors, Applied Surface Science 418 (Part B) (2017) 487 – 490.

[35] J. Byskov-Nielsen, J.-M. Savolainen, M. S. Christensen, P. Balling, Ultra-short pulse laser ablation of metals: threshold fluence, incubation coefficient and ablation rates, Applied Physics A 101 (1) (2010) 97–101.

[36] J. Bonse, H. Sturm, D. Schmidt, W. Kautek, Chemical, morphological and accumulation phenomena in ultrashort-pulse laser ablation of tin in air, Applied Physics A 71 (6) (2000) 657–665.

[37] A. Borowiec, H. Haugen, Subwavelength ripple formation on the surfaces of compound semiconductors irradiated with femtosecond laser pulses, Applied Physics Letters 82 (25) (2003) 4462–4464.

[38] J. M. Vadillo, J. M. Fernández Romero, C. Rodríguez, J. J. Laserna, Effect of plasma shielding on laser ablation rate of pure metals at reduced pressure, Surface and Interface Analysis 27 (11) (1999) 1009–1015.

[39] A. Einstein, Strahlungs-emission und -absorption nach der quantentheorie, Verhandlungen der Deutschen Physikalischen Gesellschaft 18 (1916) 318–323.

[40] O. Svelto, Principles of Lasers, 5th Edition, Springer Science+Business Media, LLC, 2010.

[41] P. A. Franken, A. E. Hill, C. W. Peters, G. Weinreich, Generation of optical harmonics, Physical Review Letters 7 (4) (1961) 118–119.

[42] W. Koechner, Solid-State Laser Engineering, sixth revised and updated Edition, Springer Science+Business Media, Inc., 2006.

[43] S. Musazzi, U. Perini, Laser-Induced Breakdown Spectroscopy Theory and Applications, Springer-Verlag Berlin Heidelberg, 2014, Ch. LIBS Instrumental Techniques, pp. 59–86.

[44] T. O. Nagy, Laser-induced in-depth spectroscopic and electrochemical analysis of protective coatings, Ph.D. thesis, University of Vienna (2014).

[45] L. Krajcarová, K. Novotný, M. Kummerová, J. Dubová, V. Gloser, J. Kaiser, Mapping of the spatial distribution of silver nanoparticles in root tissues of vicia faba by laser-induced breakdown spectroscopy (libs), Talanta 173 (2017) 28–35.

[46] A. D. Bonis, B. D. Filippo, A. Galasso, A. Santagata, A. Smaldone, R. T. and, Comparison of the performances of nanosecond and femtosecond-laser induced breakdown spectroscopy for depth profiling of anartificially corroded bronze, Applied Surface Science 302 (2014) 275–279 302 (2014) 275–279.

[47] J. Klus, P. Mikysek, D. Prochazka, P. Pořízka, P. Prochazková, J. Novotný, T. Trojek, K. Novotný, M. Slobodník, J. Kaiser, Multivariate approach to the chemical mapping of uranium in sandstone-hosted

uranium ores analyzed using double pulse laser-induced breakdown spectroscopy, Spectrochimica Acta Part B 123 (2016) 143–149.

[48] J. Klus, P. Pořízka, D. Prochazka, J. Novotný, K. Novotný, J. Kaiser, Effect of experimental parameters and resulting analytical signal statistics in laser-induced breakdown spectroscopy, Spectrochimica Acta Part B 126 (2016) 6–10.

[49] P. Pořízka, J. Klus, D. Prochazka, E. Képeš, A. Hrdlička, J. Novotný, K. Novotný, J. Kaiser, Laser-induced breakdown spectroscopy coupled with chemometrics for the analysis of steel: The issue of spectral outliers filtering, Spectrochimica Acta Part B 123 (2016) 114–120 123 (2016) 114–120.

[50] F. L. Pedrotti, L. M. Pedrotti, L. S. Pedrotti, Introduction to Optics, 3rd Edition, Prentice Hall, 2006.

[51] T. Ritzdorf, Modern electroplating ed. by M. Schlesinger, M. Paunovic, John Wiley & Sons, Inc., Hoboken, New Jersey, 2010, Ch. Monitoring and Control, pp. 527–554.

[52] A. Bengtson, Laser induced breakdown spectroscopy compared with conventional plasma optical emission techniques for the analysis of metals – a review of applications and analytical performance, Spectrochimica Acta Part B: Atomic Spectroscopy 134 (Supplement C) (2017) 123 – 132.

[53] D. A.-R. et al., Comprehensive comparison of various techniques for the analysis of elemental distributions in thin films, Microscopy and Microanalysis 17 (2011) 728–751.

[54] H. J. Eichler, J. Eichler, Laser, 6th Edition, Springer Berlin Heidelberg New York, 2006.

[55] E. Paulis, U. Pacher, M. J. Weimerskirch, T. O. Nagy, W. Kautek, Investigation of the wavelength dependence of laser stratigraphy on cu and ni coatings compared to a pure thermal ablation model, Applied Physics A (accepted manuscript).

[56] A. Kramida, Yu. Ralchenko, J. Reader, and NIST ASD Team, NIST Atomic Spectra Database (ver. 5.3), [Online]. Available: `http://physics.nist.gov/asd` [2017, September 19]. National Institute of Standards and Technology, Gaithersburg, MD. (2015).

[57] R. Weil, K. Parker, Electroless Plating - Fundamentals and Applications, William Andrew Publishing/Noyes, 1990, Ch. The Properties of Electroless Nickel, pp. 111–137.

[58] P. B. Johnson, R. W. Christy, Optical constants of transition metals: Ti, v, cr, mn, fe, co, ni, and pd, Physical Review B 9 (1974) 5056–5070.

[59] P. B. Johnson, R. W. Christy., Optical constants of the noble metals, Physical Review B 6 (1972) 4370–4379.

[60] C. Kothandaraman, S. Subramanyan, Heat and Mass Transfer Data Book, 8th Edition, New Age International, New Delhi, 2014.

[61] B. Wu, P. Liu, J. Duan, L. Deng, X. Zeng, X. Wang, Study on picosecond pulse laser ablation of cr12mov cold work mold steel, Materials and Design 110 (2016) 549–557.

[62] M. Stafe, I. Vladoiu, I. M. Popescu, Impact of the lasr wavelength and fluence on the ablation rate of aluminium, Central European Journal of Physics 6 (2008) 327–331.

[63] J. Pedarnig, 16 - application of laser-induced breakdown spectroscopy to the analysis of secondary materials in industrial production, in:

M. Baudelet (Ed.), Laser Spectroscopy for Sensing, Woodhead Publishing, 2014, pp. 496 – 521.

[64] P. Yaroshchyk, R. J. Morrison, D. Body, B. L. Chadwick, Quantitative determination of wear metals in engine oils using libs: The use of paper substrates and a comparison between single- and double-pulse libs, Spectrochimica Acta Part B: Atomic Spectroscopy 60 (11) (2005) 1482 – 1485.

[65] R. Sanginés, V. Contreras, H. Sobral, A. Robledo-Martinez, Optimal emission enhancement in orthogonal double-pulse laser-induced breakdown spectroscopy, Spectrochimica Acta Part B: Atomic Spectroscopy 110 (Supplement C) (2015) 139 – 145.

Nomenclature

α_{eff}	effective absorption coefficient, [μm^{-1}]
α_{opt}	optical absorption coefficient, [μm^{-1}]
α_{th}	thermal absorption coefficient, [μm^{-1}]
λ	wavelength, [nm]
τ	pulse length, [ns]
θ	beam divergence, [rad]
D	spot-diameter $D^2 = 2w_0^2 \ln \frac{F}{F_{th}}$, [$cm^2$]
d_0	Gaussian beam diameter, [μm]
F	maximum fluence [J/cm^2]
F_{th}	threshold fluence [J/cm^2]
$F_{\text{th}}(1)$	threshold fluence at one pulse [J/cm^2]
$F_{\text{th}}(N)$	threshold fluence at N pulses [J/cm^2]
h	average ablation rate, [μm/pulse]
L_{eff}	$\frac{1}{\alpha_{\text{eff}}}$, [$\mu m$]
L_{opt}	optical penetration depth, [μm]
L_{th}	thermal diffusion length, [μm]
M^2	beam quality factor
N	number of laser pulses
TEM_{00}	ground transverse electromagnetic mode
w_0	Gaussian beamwaist radius (in the focal plane), [μm]
z_{R}	Rayleigh length, [cm]
AES	atomic emission spectroscopy

BBO ..... beta-barium borate
BSE ..... backscattered electrons
CCD ..... charge-coupled device
DOF ..... depth of focus
EDX ..... energy-dispersive X-ray spectroscopy
FWHM ..... full width at half maximum
GDOES ..... glow-discharge optical emission spectroscopy
ICCD ..... intensified charge-coupled device
ICP-OES .... inductively coupled plasma atomic emission spectroscopy
IR ..... infrared light (1064 nm)
KDP ..... potassium dihydrogen phospate
LIBS ..... laser-induced breakdown spectroscopy
LIPS ..... laser-induced plasma spectroscopy
MCP ..... microchannel plate
Nd:YAG ..... neodymium doped yttrium-aluminium-garnet
PBS ..... polarising beam splitter
PD ..... photodiode
PDA ..... photodiodes array
PMT ..... photomultiplier tube
Q-switch ..... quality-switch
SEM ..... scanning electron microscopy
SHG ..... second harmonic generation (532 nm)
VIS ..... visible light (532 nm)
XRF ..... X-ray fluorescence

List of Figures

List of Tables

Appendix A

Threshold fluence and incubation coefficient determination

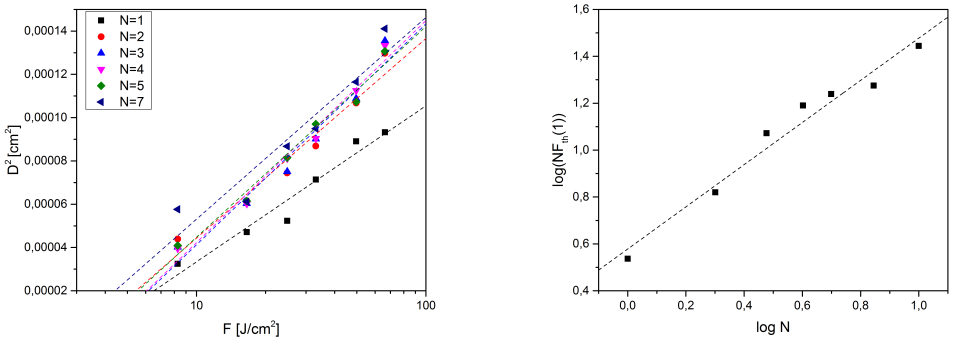

(a) **(b)**

Figure A.1: Determination of threshold fluence and incubation coefficient at Ni-2 sample at 532 nm.

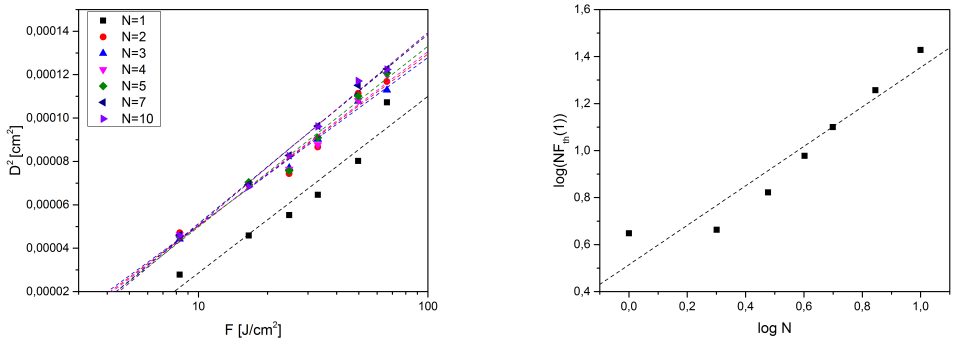

(a) **(b)**

Figure A.2: Determination of threshold fluence and incubation coefficient at Ni-3 sample at 532 nm.

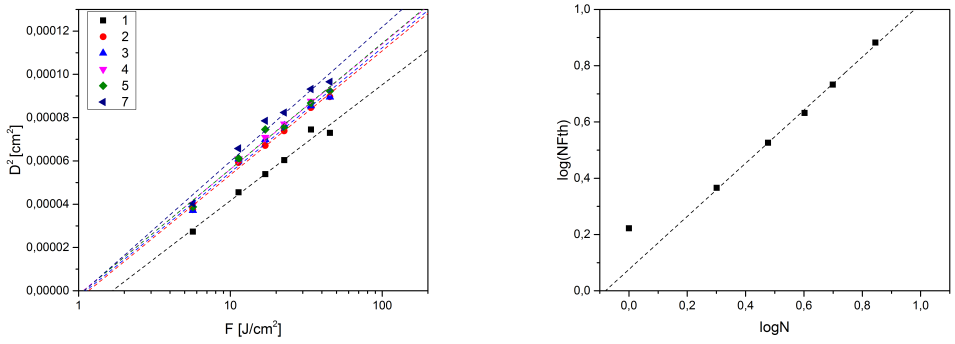

(a) **(b)**

Figure A.3: Determination of threshold fluence and incubation coefficient at Ni-1 sample at 1064 nm.

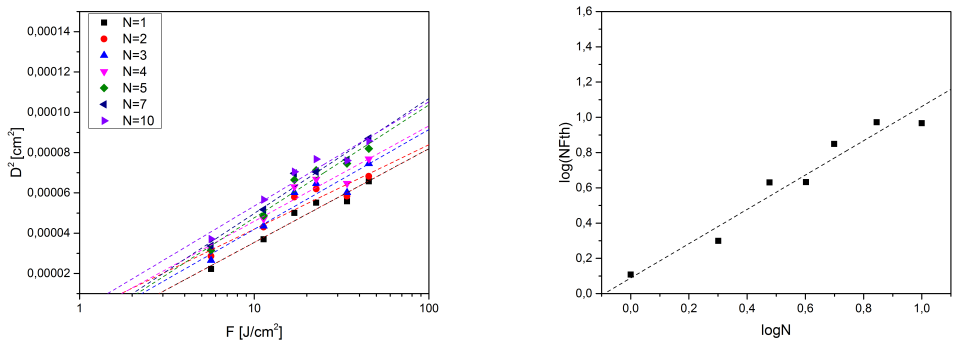

(a) **(b)**

Figure A.4: Determination of threshold fluence and incubation coefficient at Ni-2 sample at 1064 nm.

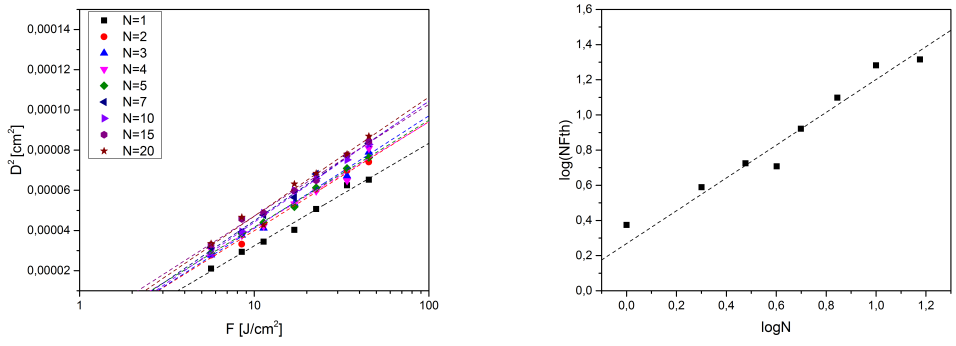

(a) **(b)**

Figure A.5: Determination of threshold fluence and incubation coefficient at Ni-3 sample at 1064 nm.

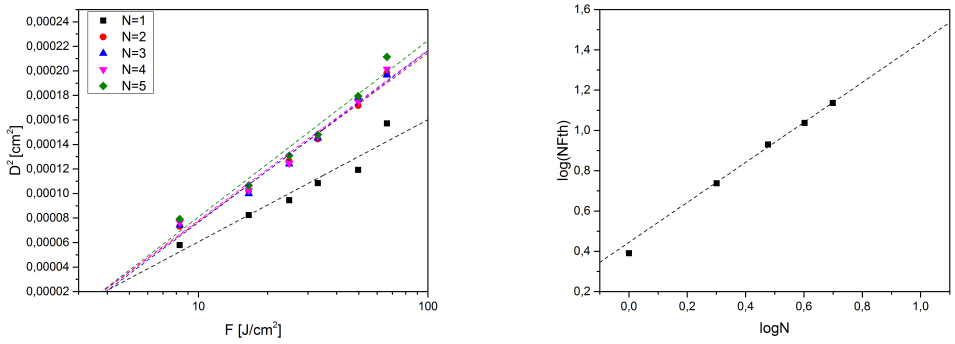

(a) **(b)**

Figure A.6: Determination of threshold fluence and incubation coefficient at NiP-1 sample at 532 nm.

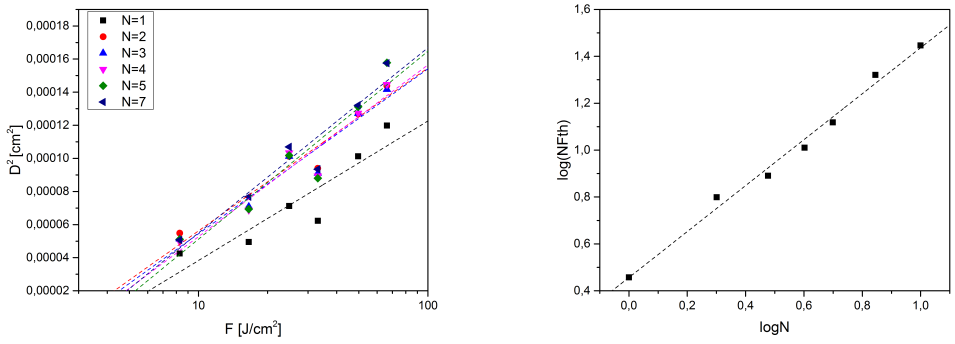

(a) **(b)**

Figure A.7: Determination of threshold fluence and incubation coefficient at NiP-2 sample at 532 nm.

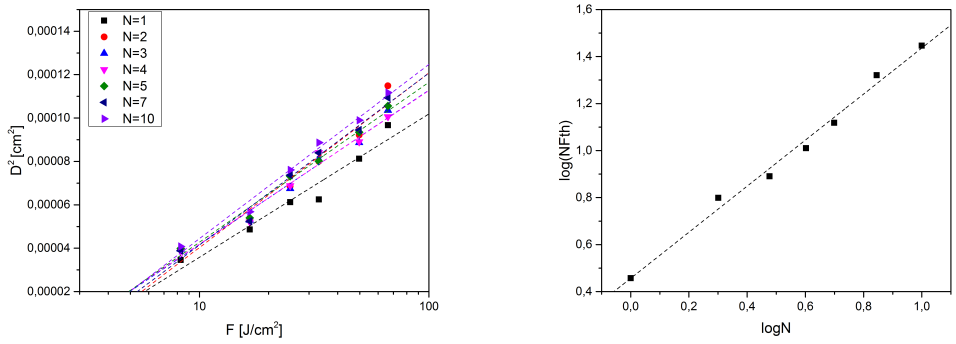

(a) **(b)**

Figure A.8: Determination of threshold fluence and incubation coefficient at NiP-3 sample at 532 nm.

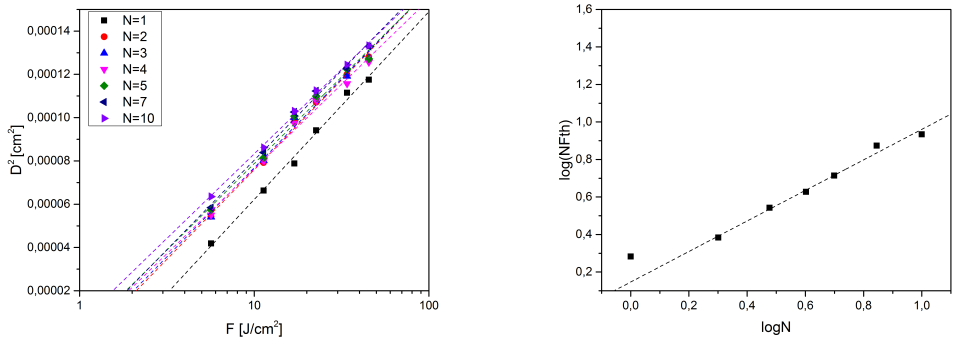

(a) **(b)**

Figure A.9: Determination of threshold fluence and incubation coefficient at NiP-1 sample at 1064 nm.

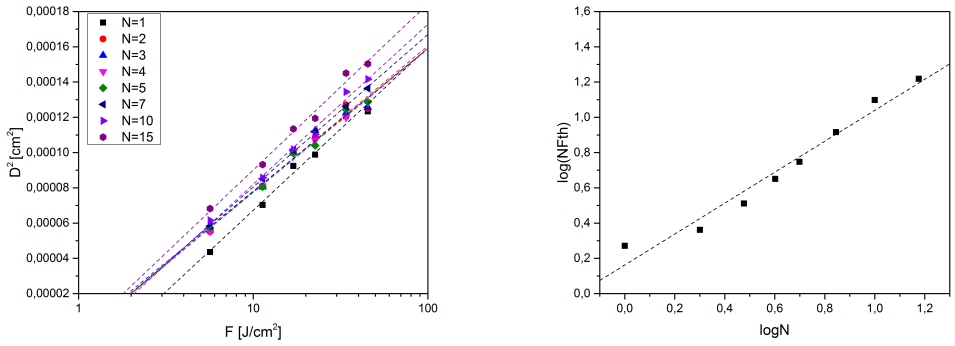

(a) **(b)**

Figure A.10: Determination of threshold fluence and incubation coefficient at NiP-2 sample at 1064 nm.

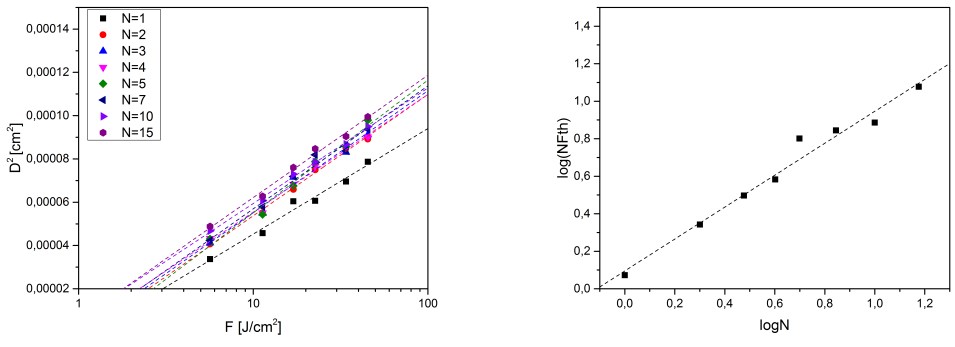

(a) **(b)**

Figure A.11: Determination of threshold fluence and incubation coefficient at NiP-3 sample at 1064 nm.

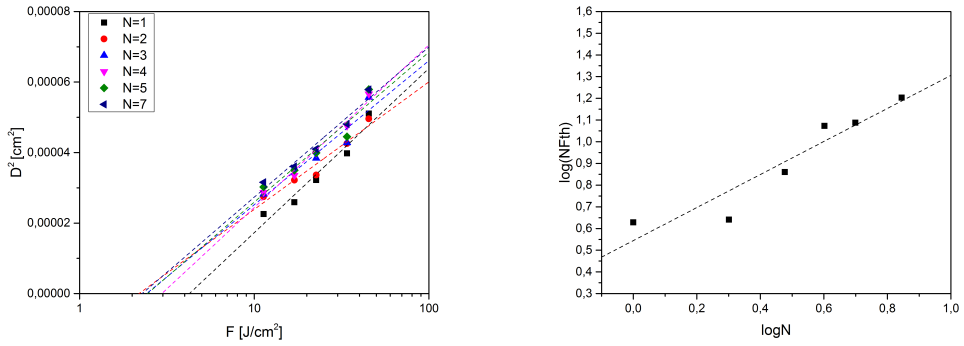

(a) **(b)**

Figure A.12: Determination of threshold fluence and incubation coefficient at Cu-2 sample at 1064 nm.

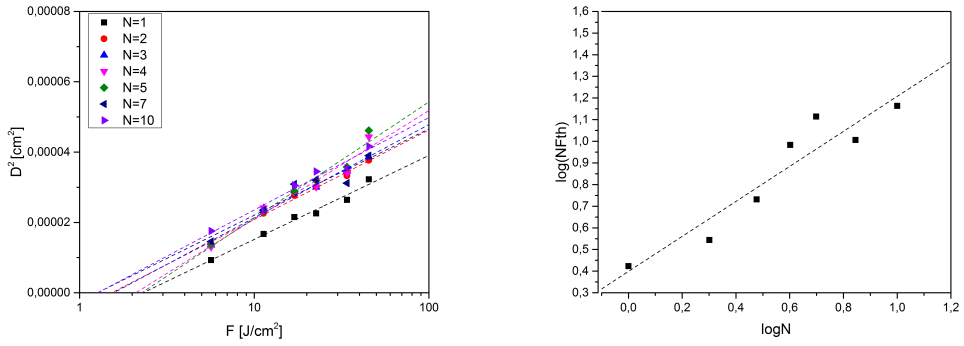

(a) **(b)**

Figure A.13: Determination of threshold fluence and incubation coefficient at Cu-3 sample at 1064 nm.

Appendix A. Threshold fluence and incubation coefficient determination

Appendix B

Acknowledgments

I would like to thank ...

... Prof. Wolfgang Kautek for giving me an opportunity to work in his research group on the interesting, promising and up to date project and for supervising my thesis.

... Dr. Tristan O. Nagy for his excellent supervising, for being patient, encouraging, for sharing his experience and knowledge, for spending a lot of time for teaching me, for motivating and pushing me in a right moment.

... Ulrich Pacher for his invaluable technical assistance, terrific patience and being helpful at any time.

... Martina Hofmann for the preparation of the cross-section for SEM and EDX-Spectroscopy, Dr. Stephan Puchegger for his assistance with SEM.

... Erwin Schrödinger Society for Nanosciences and Bundesministerium für Verkehr, Innovation und Technologie for the partial financial support and making possible the presentation of this work at EMRS Spring Meeting in Strasbourg.

. . . Deutsche Bunsen-Gesellschaft für physikalische Chemie for providing me the Student Travel Grant, supported my participation and the presentation of this work at Bunsentagung 2017.

. . . my family and especially my mother for making my education possible, for her unconditional love, for accepting my decision to study abroad, for everything she has done for me and my live. I will never forget it.

. . . my husband Christoph for always believing in me and encouraging in the dark time of frustration.

. . . my friends for supporting my ideas and accompanying me during this journey.